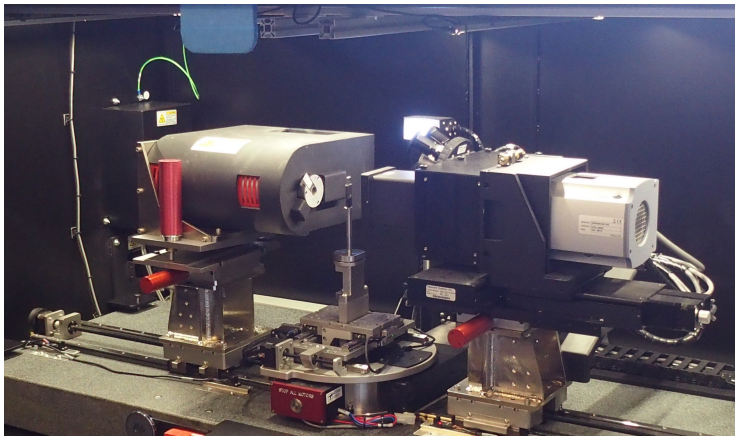


SIMULATED PHASE CONTRAST TOMOGRAPHY EXPERIMENTS USING TOTAL VARIATION REGULARIZATION



RASMUS DALGAS RASMUSSEN
s093085

DTU Compute - Kongens Lyngby
MSc-2014-Spring

Supervisors: Per Christian Hansen, Professor
Henning Friis Poulsen, Professor
Yiqiu Dong, Assistant Professor
Jakob Sauer Joergensen, Postdoc



Technical University of Denmark
Department of Applied Mathematics and Computer Science
Building 322, DK-2800 Kongens Lyngby, Denmark
Phone +45 4525 3031 , Fax +45 4588 1399
compute@compute.dtu.dk
www.compute.dtu.dk MSc-2014-Spring

SUMMARY

In this thesis, phase contrast tomographic experiments are simulated in order to test and compare different variations of the reconstruction methods related to phase contrast tomography(PCT).

Computed tomography formulated as both a continuous and discrete model is presented. Different reconstruction methods, including analytical and iterative methods are also presented with some examples. This leads to a presentation of the regularization methods, where total variation (TV) regularization is the main focus for this project.

A forward model for the PCT experimental set-up called *free space propagation* is presented and implemented, in order to simulate experimental data. Phase retrieval techniques, which are used when reconstructing PCT data, are also presented and implemented. From these techniques a selection of complete PCT reconstruction methods are defined and put into the formulation of TV regularization. In order solve the defined TV regularization problems an optimization algorithm is implemented, which is set up to handle the PCT reconstruction methods.

Finally the optimization algorithm is used to solve different types of simulated experiments using the different methods. First the PCT methods are tested against the standard absorption based tomography method, to show some examples where PCT can be advantageous. Next the different PCT methods are tested for different scenarios and compared in order to identify the advantages and disadvantages of the different techniques.

PREFACE

This thesis was prepared at the department of Applied Mathematics and Computer Science at the Technical University of Denmark in fulfilment of the requirements for acquiring an M.Sc. in Civil Engineering. The work on this project corresponds to 30 ECTS point and was conducted from February to June 2014.

I would like to thank all of my supervisors: prof. Per Christian Hansen, prof. Henning Friis Poulsen, asst. prof. Yiqiu Dong and postdoc Jakob Sauer Jørgensen for suggestions, guidance and inputs throughout the project. I would especially like to thank Jakob Sauer Jørgensen for his help and talks about mathematics and computer science. Besides that I would like to thank my friends and family for support and especially my girlfriend Sisse Kongskov for her help in the tough periods.

Lyngby, 30-June-2014



RASMUS DALGAS RASMUSSEN
s093085

Contents

SUMMARY	i
PREFACE	iii
NOMENCLATURE	vii
1 INTRODUCTION	1
2 COMPUTED TOMOGRAPHY	3
2.1 X-ray tomography	5
2.1.1 Continuous model and analytical reconstruction	6
2.1.2 Discrete model and algebraic reconstruction	9
2.1.3 Regularization	13
2.1.4 Measurement noise	15
2.2 Summary	16
3 PHASE CONTRAST FORWARD MODEL	17
3.1 Phase contrast	18
3.2 Free space propagation	20
3.3 Discretization and examples in 2D	24
3.3.1 Phantom	27
3.4 Summary	28

4	PHASE RETRIEVAL	31
4.1	Phase retrieval methods	32
4.1.1	The CTF method	32
4.1.2	The duality method	35
4.2	Summary	36
5	PHASE CONTRAST TOMOGRAPHY	37
5.1	Two stage reconstruction method	37
5.2	Algebraic combined method	39
5.3	Summary	41
6	TOTAL VARIATION REGULARIZATION	43
6.1	Implementation of Chambolle Pock algorithm	43
6.2	TV for Phase contrast data	48
6.3	Summary	49
7	SIMULATIONS	51
7.1	Classical CT vs phase contrast tomography	53
7.2	PCT methods for different materials	57
7.3	PCT methods for different noise levels	62
7.4	Summary	64
7.5	Discussion	64
8	CONCLUSION AND FUTURE WORK	67
8.0.1	Future work	68
	Bibliography	69

NOMENCLATURE

List of symbols

λ	Wavelength of X-rays.
E	Energy of X-rays.
I_0	Intensity of X-ray before interaction with object.
I_L	Intensity of X-ray after interaction with object.
\mathbf{x}	Cartesian coordinate vector.
$f(\mathbf{x})$	Continuous object in Cartesian coordinates.
x_i	Cartesian coordinate in dimension i .
\mathcal{R}	Radon transform operator.
δ_{Dirac}	Dirac delta function.
t	Translational variable from the Radon transform, perpendicular to the direction of the X-rays.
θ	Angular parameter from the Radon transform.
$p_{\theta_i}(t)$	Projection through Radon transform, for angular variable value θ_i with integer i .
$p_{\theta}(t)$	Sinogram of projections through Radon transform.
$\mathcal{F} / \mathcal{F}^{-1}$	Fourier transform operator / inverse Fourier transform operator.
ω	Frequency vector for Fourier space frequencies.
N_{θ}	Number of discrete angles for angular parameter θ .
N_t	Number of discrete values of translation variable t .
$\Psi(\omega)$	Filter function in Fourier space.
N	Number of pixels in each coordinate direction.
$P_{i,j}$	Pixel expansion function.
p_n	Pixel expansion function in single index notation n .
$U_{i,j}$	Discrete object value in pixel i, j .
u_n	Discrete object value in single index notation n .
b_m	Discrete measurement of X-ray following line L_m .
$a_{m,n}$	Distance travelled by ray m through pixel n .
A	Projections matrix of size $M \times N^2$ with elements $a_{m,n}$.
T_1, T_2	Symmetric positive definite matrices defining the SIRT methods.
\mathcal{I}	Identity matrix.

$T(u)$	Data fidelity term in the regularization formulation.
$R(u)$	Regularizer in the regularization formulation.
D	Finite difference approximation of the derivative operator.
α	Regularization parameter in the regularization formulation.
J_{TV}	Total variation analytical operator.
$R_{TV}(u)$	Total variation discrete regularizer.
D_n	Local derivative in pixel n .
d	Thickness of 3D object.
n_i	Refractive index of material.
δ	Refractive index decrement.
β	Absorption index.
$B(\mathbf{x})$	Absorption image from one X-ray projection.
$\phi(\mathbf{x})$	Phase shift image from one X-ray projection.
$T(\mathbf{x})$	Transmittance function.
R	Distance from object to detector.
q	Smallest detectable element.
$P^R(\mathbf{x})$	Fresnel propagator.
$I^R(\mathbf{x})$	Intensity image.
p_s	Pixel size on the detector.
c	Speed of light.
h	Planck's constant.
$B_\theta(t)$	Absorption data.
$\phi_\theta(t)$	Phase shift data.
β_v, δ_v	Vectors with discrete absorption index and refractive index decrement, respectively.
B_v, ϕ_v	Vectors with absorption data and phase shift data, respectively.
$T_\theta(t)$	Transmission data.
$I_\theta^R(t)$	Intensity data.
T_v, I_v^R	Vectors with discrete transmission and intensity data, respectively.
C, S	Diagonal matrices for linear phase retrieval model.
G	Matrix for CTF phase retrieval model.
σ	Proportionality between absorption and phase shift data.
W	Matrix for CTF duality phase retrieval model.
Q	Matrix for AC2R method.

Abbreviations

CT	Computed Tomography.
PCT	Phase Contrast Tomography.
FBP	Filtered Back Projection.
IR	Iterative Reconstruction.
ART	Algebraic Reconstruction Technique.
SIRT	Simultaneous Iterative Reconstruction Techniques.
TV	Total Variation.
ABT	Absorption Based Tomography.
CTF	Contrast Transfer Function.
TS	Two Stage.
AC	Algebraic Combined.
TS2R	Two Stage method with two R distances.
TSD	Two Stage method with Duality assumption.
AC2R	Algebraic Combined method with two R distances.
ACD	Algebraic Combined method with Duality assumption.
CP	Chambolla and Pock optimization algorithm.

The scientific research of Computed Tomography (CT) began in the 60's and 70's [1] and is still a developing research topic in many universities around the world. The origin of CT was within the perspective of using it for analysis of biological tissue, directed at both treatment and research of mainly the human body. With the advancement of synchrotrons and more coherent X-ray sources the use of CT has spread to other research areas. For industrial applications, in materials science within physics and biological research, among other things, this method has also proven a valuable analysis tool. Increasing demand of higher resolution, lower X-ray doses, better distinction between similar tissues and reduced time consumption places high demands on the acquisition of data and mathematical reconstruction methods.

Recent development in laboratory X-ray sources have made partially coherent high energy X-rays acquirable on relatively small experimental set-ups, compared to the synchrotrons. This opens up for techniques which are not usually used in lab facility, such as Phase Contrast Tomography (PCT) which is the subject of this thesis. At the frontpage an image of a laboratory X-ray source from DTU physics is shown.

The main idea behind PCT is based on the refractive effects of X-rays when passing through an object. In the classical set up, the X-ray passing through the medium is mathematically modelled as purely absorption based, where the refractive behaviour is seen as negligible. For PCT, the refraction is modelled as a phase change of the travelling X-ray waves. By expanding the absorption model to include refraction, the model becomes more detailed and advanced, with the aim to produce more precise and exact scanning results. Therefore PCT could be used to produce better results than absorption based tomography for some experiments. Since the model, and hence the problem to be solved,

becomes more complicated this is not necessarily a method which is desirable for all purposes.

The method for solving CT problems is called reconstruction, and reconstructions are also an important part of solving PCT problems. There exists a series of reconstruction methods based on either analytical or discrete mathematical formulations, with different focuses such as efficiency, data acquisition, prior knowledge among other things. For this project the focus is to use Total Variation (TV) regularization as the reconstruction technique, since the specimen examined with X-rays often are piecewise constant and since it has been used to produce some good results for both CT [2] and PCT [3].

The main focus for this project to simulate different PCT experiments and show what strengths and weaknesses are related to PCT and the different takes on this method. Some simulated PCT experiments should demonstrate problems where PCT method would be valuable or maybe even necessary when compared with the classical CT method. Other simulated experiments are carried out in order to test and compare different variations of PCT and especially what the strengths and limits of these are. In this way, a thorough comparison of different PCT variations could make a basis for choosing the experimental set up and reconstruction method that is best suited for a real life experiment.

All code and simulations has been carried out in MATLAB. Functions from packages, besides the standard library tools are mentioned when used. The implemented code, along with supplementary packages, can be download via Dropbox ¹.

¹dl.dropboxusercontent.com/u/4368314/Matlab_Code_Msc_Rasmus_Dalgas.zip

COMPUTED TOMOGRAPHY

Computed tomography, with a focus on standard absorption based tomography, is presented with a short historic introduction. X-ray tomography and data acquisition methods are also introduced. Different reconstruction methods, including both analytical and iterative, are presented with a few examples. Finally regularization and measurement noise is also mentioned.

From a mathematical point of view, the task of calculating the interior of an object from measured lower dimensional projections is called *reconstruction*. The reconstruction problem is a so called inverse problem, where we derive some model to describe the behaviour of the travelling X-rays, measure the X-rays after they have passed through the object and try to calculate what object fits the measurements through the model. See [Figure 2.1](#) for a schematic overview.

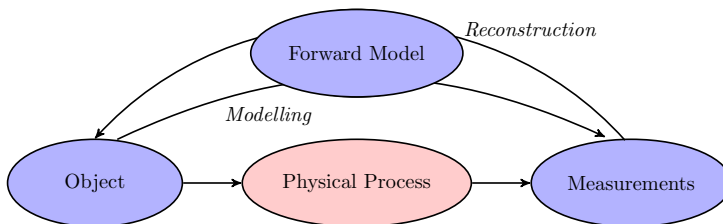


Figure 2.1: The inverse problem aims to reconstruct the *Object*, which corresponds best, in some sense, to the *Measurements*, which are recorded through some not completely known *Physical Process*. In the ideal situation the *Forward Model* used for the reconstruction is very similar to the physical process, though this could require the model to be highly complex, which is undesirable for several reasons.

Inverse problems, such as the reconstruction problem, are often ill-posed. Ill-posed problems are problems which does not fulfil the conditions for a well-posed problem. Well-posed problems were defined by Hadamard [4] by three conditions:

- Existence: Does a solution to the problem exist?
- Uniqueness: Is the solution unique?
- Stability: Is the solution stable?

For reconstruction problems these conditions can all be broken in different cases. If the measurements are affected by noise, there might not exist any solution which fits the measurements exactly. If the number of measurement data points is less than the number of variables we solve for, there can be series of solutions which fits the measurements, not one unique solution. Finally the model can be unstable with respect to changes in the data, which means that the solution could change dramatically for small changes in the measurements. All three conditions should be kept in mind when solving reconstruction problems, since they are essential when deciding for the solution method.

The reconstruction problem was a research topic of the Bohemian mathematician Johann Radon who published a paper about the reconstruction problem in 1917, where he showed that a unique solution can be obtained from a complete series of line integrals through an object. However practical solution methods was not developed until about 50 years later [1], where the development of CT as we know it today started.

The first scanners were so called *pencil beam* scanners which emits single X-ray beams. The X-ray source is rotated around the object, perpendicular to the beam direction, and for different angles the remaining X-ray intensity is measured in a single detector. In order to obtain sufficient data for the reconstruction, the X-ray source is translated linearly in the direction perpendicular to the beam direction and several measurements are thereby recorded for each angle [1]. See [Figure 2.2](#) for a 2D model sketch of the pencil beam.

The pencil beam scanner only allows us to measure a single ray at a time, which is a very time costly drawback. This drawback lead to a development of the *fan beam* scanner. The fan beam scanner emits X-rays in a fan with some angular width, rather than a single ray, and thus a series of detectors, instead of just one, is needed. See [Figure 2.3](#) for a 2D model sketch of the fan beam geometry. This method speeds up the data acquisition and reduces the total scan time duration significantly which is desirable for many practical purposes. Today most industrial CT scanners uses the fan beam (or 3D cone beam) method

since speed is critical.

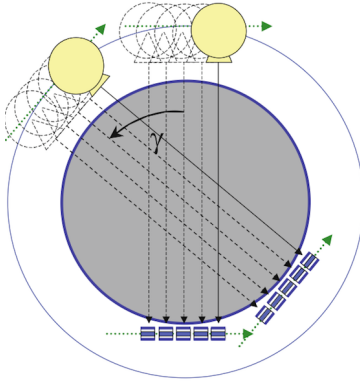


Figure 2.2: Pencil Beam geometry.
Figure taken from [1].

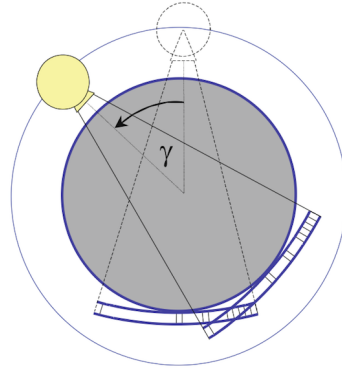


Figure 2.3: Fan Beam geometry.
Figure taken from [1].

A problem with the fan beam scanner geometry, is the more complicated geometry, since the rays are not parallel. For some physical set-ups the parallel rays are still required, for example synchrotron facilities. Therefore a parallel beam method is used, which is similar to the the pencil beam scanner, but instead of one beam, several parallel beam are projected simultaneously.

2.1 X-ray tomography

Tomography is a technique used within a wide variety of natural sciences, for example geology, biology and medical science. The technique utilizes the effects of travelling electromagnetic waves, light or sound waves for example, to section an object of interest. The waves used in CT scanners are X-ray waves, which are in electromagnetic waves with a wavelength in the range $\lambda \in [3 \cdot 10^{-9}, 10^{-6}]$ (m), corresponding to energies in the range $E \in [1, 400]$ (KeV) [5].

The most common X-ray tomography method, used in for example medical equipment, is the absorption based method. For this method the transmission, especially the absorption, of the X-rays through an object is modelled by the Lambert-Beer law. This law models the attenuation of the X-rays along lines through some object. For a Cartesian coordinate vector \mathbf{x} and the coefficient of attenuation for the object described as a function f , the law can be mathemat-

ically stated as [5]

$$I_L = I_0 \exp \left(- \int_L f(\mathbf{x}) \, d\mathbf{x} \right). \quad (2.1)$$

Here the I_L is the intensity of X-ray L after interaction with the object. In this setting \mathbf{x} could be any dimension larger than one. Rearranging (2.1) we arrive at

$$\log \left(\frac{I_0}{I_L} \right) = \int_L f(\mathbf{x}) \, d\mathbf{x}, \quad (2.2)$$

which is called the projection measurement. These projections are the available data we will have from a series of measurements, and the attenuation coefficient f is what we want to find, i.e. the inverse problem of tomography.

The detectors of most CT systems are scintillator detectors, which consist of a scintillator and a photon detector. The scintillator converts the short-wave X-rays into long-wave electromagnetic waves [1] which can be recorded by a photon detector, for example a CCD. The recorded photon count can be related to the intensity of the X-ray after the object, I_L . The original intensity of the X-ray is known, I_0 , and together this gives us the projection measurements.

2.1.1 Continuous model and analytical reconstruction

The analytical reconstruction methods are based on continuous measurements and continuous reconstructions. For real life problems the measurements will be discrete, though for the mathematical theory the continuous model is used. A central part of the analytical reconstruction methods is the *Radon* transform. This transform relates the angular measurements to the projections through a line integral, similar to Lambert-Beer law (2.2).

A 2D object defined in Cartesian coordinates, x_1 and x_2 , as the continuous function $f(x_1, x_2)$ can be parametrized by an angular parameter $\theta \in [0, \pi[$ and the translational parameter $t \in \mathbb{R}$ through the relation

$$t = x_1 \cos(\theta) + x_2 \sin(\theta). \quad (2.3)$$

Given this parametrization the Radon transform \mathcal{R} can be written in one of the following ways:

$$\begin{aligned} \mathcal{R}f(t, \theta) &= \int_{-\infty}^{\infty} f(t \cos(\theta) - \tau \sin(\theta), t \sin(\theta) + \tau \cos(\theta)) \, d\tau \\ &= \int_{-\infty}^{\infty} \int_{-\infty}^{\infty} f(x_1, x_2) \delta_{\text{Dirac}}(t - x_1 \cos(\theta) - x_2 \sin(\theta)) \, dx_1 \, dx_2. \end{aligned}$$

Where δ_{Dirac} is the Dirac delta function. This transform also generalizes to higher dimensions > 2 , where the integration is over hyperplanes of dimension $n - 1$. For each angular value $\theta_i \in [0, \pi[$ this transform corresponds to a projection p

$$p_{\theta_i}(t) = \mathcal{R}f(t, \theta_i).$$

A series of projections is often called a sinogram. These projections are the measurements as mentioned in the previous section. In theory the translational parameter $t \in \mathbb{R}$ can be any real number, though in practice since the object of interest only has some finite dimensions this parameter will only have some finite range of values.

Relating this to the schematic overview of the inverse problem in [Figure 2.1](#), we now have the data measured by the detector, i.e. the *Measurements*. The measurements are assumed to follow the *Forward model*, Lambert-Beer law, through a Radon transform, and the next step is to reconstruct by solving the inverse problem.

Filtered back projection

The most common analytical reconstruction method is called filtered back projection (FBP). This method filters the projections in the Fourier domain followed by a back projection to the object domain in the Cartesian coordinates [\[1\]](#). This method can be written up as a three step procedure:

$$\begin{aligned} \text{Fourier transform} \quad & \hat{p}_\theta(\omega) = \mathcal{F}(p_\theta(t)) = \int_{-\infty}^{\infty} p_\theta(t) e^{-2\pi i t \omega} dt \\ \text{Filtering} \quad & p_\theta^f(t) = \mathcal{F}^{-1}(\hat{p}_\theta(\omega)|\omega|) = \int_{-\infty}^{\infty} \hat{p}_\theta(\omega)|\omega| e^{2\pi i t \omega} d\omega \quad (2.4) \\ \text{Back projection} \quad & f(x_1, x_2) = \int_0^\pi p_\theta^f(t) d\theta = \int_0^\pi p_\theta^f(x_1 \cos(\theta) + x_2 \sin(\theta)) d\theta \end{aligned}$$

Here the parametrization [\(2.3\)](#) is used. \mathcal{F} denotes the 1D Fourier transform along t and the Fourier transformed variables are marked with $\hat{\cdot}$. This specific filter in this method is needed to secure the reconstruction of the object to be exact. That is, for a complete sinogram where measurements are collected from all angles and translations, the object can be reconstructed exactly, using FBP.

As mentioned above the measurements will be discrete in real life, and so this continuous formulation has to be discretized in order to be useful in practice. In MATLAB this can be done using the function `radon`. This calculates the Radon transform of a discrete object. Filtered back projection can also be carried out in MATLAB, this can be done using the function `iradon`.

In [Figure 2.4](#) an object called the Shepp-Logan phantom, which resembles a

cross section of a brain, is transformed to a series of projections (the sinogram) and reconstructed using FBP. The actual Shepp-Logan phantom is a 3D model, but to make it simple a 2D example is presented here, since the techniques can be generalized to 3D.

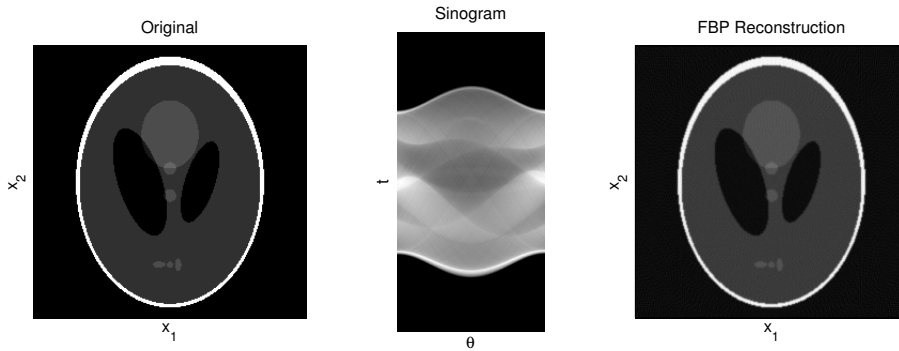


Figure 2.4: Radon transform and FBP on Shepp-Logan phantom (256×256 pixels). $N_\theta = 180$ equidistant discrete angles in $[0^\circ, 179^\circ]$ and $N_t = 367$ t -values for each discrete angle.

The FBP method presented in the three steps (2.4) has a problem when data becomes noisy data. The filtering process in the Fourier domain filters the data according to the absolute value of the frequencies i.e. high frequency data is amplified and low frequency data is dampened. The problem is that the measurements are inevitably affected by noise, so high frequency noise will be amplified when reconstructing using FBP. A way to handle this problem is to modify the $|\omega|$ filter, also called the ramp filter, to a filter which either amplifies the high frequencies less or even dampens them. A series different filter functions $\Psi(\omega)$ that is typically used for this, are shown in Figure 2.5.

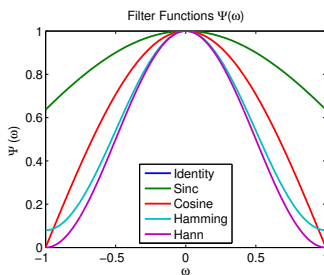


Figure 2.5: Functions for filter modification, frequencies between -1 and 1.

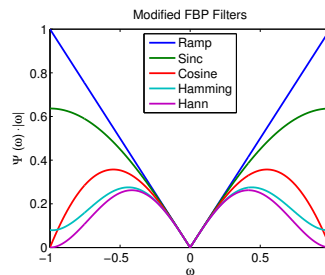


Figure 2.6: Modified filters, frequencies between -1 and 1.

These functions are multiplied to the ramp filter, in the *filtering* step in (2.4), such that the final filter becomes $\Psi(\omega) \cdot |\omega|$. These filters are visualized in Figure 2.6, where $\Psi(\omega)$ is just the identity for the ramp filter. When introducing the filter functions it should be noted that the FBP method loses its exactness.

To show the effects of these filters in reconstructions, Gaussian white noise have been added to the sinogram in Figure 2.4 and the different filters have been used in the reconstruction process. To compare the different reconstructions numerically an error-measure is needed. Here a relative error measure e is used, defined as

$$e(u) = \frac{\|u - u^*\|_2}{\|u^*\|_2} \cdot 100, \quad (2.5)$$

where vector u is the FBP solution, vector u^* is the original image and $\|\cdot\|_2$ is the two-norm. In Figure 2.7 the reconstructions of the (256×256) pixel Shepp-Logan phantom is shown with corresponding relative error.

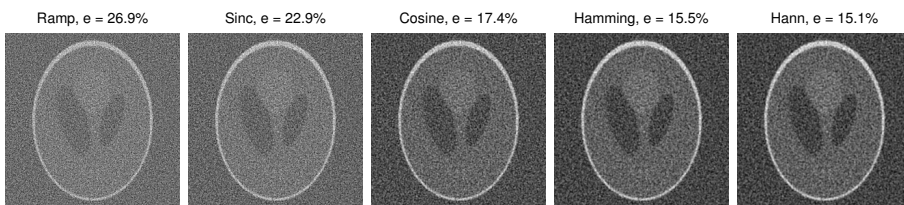


Figure 2.7: FBP solutions using different filters on data with normal distributed noise added, of a relative magnitude level at 25%.

For this specific problem the Hann filter gave the best numerical result, though this is very problem dependant. The performance of the filters is also highly related to the magnitude of the noise, for example for this specific problem the Ramp filter gives the best numerical result for a low 5% noise level and the cosine filter the best result for a 10% noise level.

2.1.2 Discrete model and algebraic reconstruction

As opposed to the analytical solution methods presented in the previous section, there is also a series of discrete solution methods which can be used to reconstruct the object from a set of measurements. For these methods both the object space and the reconstruction space is discrete. The model used is a linear model which follows from the discretization.

The discretization of the object space is based on an expansion with respect to a set of expansion functions. In this case the pixel (for 2D or voxel for 3D)

expansion functions is used as in [6]. Here, similar to the analytical reconstruction, only the 2D case is considered for simplicity. The object space is separated into $N \times N$ equal-sized pixels. For pixel (i, j) the pixel expansion function is:

$$P_{i,j}(\mathbf{x}) = \begin{cases} N^2 & \text{if } \mathbf{x} \in [x_1^{(i-1)}, x_1^{(i)}] \times [x_2^{(j-1)}, x_2^{(j)}], \\ 0 & \text{else,} \end{cases} \quad i, j = 1, 2, \dots, N.$$

With pixel values $U_{i,j}$ the expansion can be written as:

$$f(\mathbf{x}) = \frac{1}{N^2} \sum_{i,j=1}^N U_{i,j} P_{i,j}(\mathbf{x}) = \frac{1}{N^2} \sum_{n=1}^{N^2} u_n p_n(\mathbf{x}) \quad \text{where } n = i + (N-1)j. \quad (2.6)$$

Here single index notation $n = 1, 2, \dots, N^2$ is introduced.

As mentioned in the beginning of section 2.1 the projection measurements are integrals along lines through the object. The discrete measurements becomes:

$$b_m = \log \left(\frac{I_0}{I_{L_m}} \right) = \int_{L_m} f(\mathbf{x}) \, d\mathbf{x} \quad m = 1, 2, \dots, M.$$

Inserting the discrete expansion of the object space this becomes:

$$b_m = \int_{L_m} f(\mathbf{x}) \, d\mathbf{x} = \int_{L_m} \frac{1}{N^2} \sum_{n=1}^{N^2} u_n p_n(\mathbf{x}) \, d\mathbf{x} = \frac{1}{N^2} \sum_{n=1}^{N^2} u_n \int_{L_m} p_n(\mathbf{x}) \, d\mathbf{x}.$$

The integral over the basis functions $p_n(\mathbf{x})$ can be determined by introducing $a_{m,n}$: the distance travelled by ray m through pixel n . A sketch of this is shown in Figure 2.8. Inserting $a_{m,n}$ into the integral becomes $\int_{L_m} p_k(\mathbf{x}) \, d\mathbf{x} = N^2 a_{m,n}$. The discrete model therefore becomes

$$b_m = \sum_{n=1}^{N^2} u_n a_{m,n} \quad m = 1, 2, \dots, M.$$

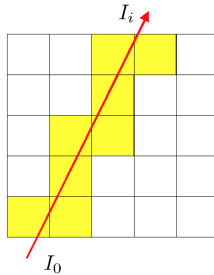


Figure 2.8: Line intersection method sketch, that shows the pixels intersected by a single x-ray. Taken from [6].

The relation between measurements b and the object u is linear, so by creating matrix A with element values $a_{m,n}$ such that $A = \{a_{m,n}\}_{m=1,\dots,M,n=1,\dots,N^2}$ we can write this as a linear system

$$Au = b. \quad (2.7)$$

In this linear system b and u are column vectors of measurements and pixel-values, respectively. If ray m does not intersect with pixel n , $a_{m,n}$ is 0 and since this is relatively typical the matrix A is sparse. For a series of measurements $b_m, m = 1, \dots, M$ and a known scanning geometry, where we know which pixel is intersected by which X-ray we can set up A and we have a linear discrete model ¹.

This model assumes that the object is piecewise constant within each pixel, which is an approximation of the real world that becomes better for smaller pixel sizes. With this model we have arrived at a linear inverse problem.

Iterative Reconstruction

The system matrix A in (2.7) often becomes large when we have a lot of data combined with a desire for high resolution results, i.e. many pixels. Therefore Iterative Reconstruction (IR) methods, or also called algebraic method, are typically used for solving the linear system, rather than classical Gaussian elimination. There are two main classes within iterative: Algebraic Reconstruction Technique (ART) and Simultaneous Iterative Reconstruction Techniques (SIRT).

The ART method is a row action method, which iterates row by row [8]. So in one total iteration, k , the method steps through all of the M rows of the system matrix A . For the k 'th iteration and m 'th row of the system matrix A denoted as a_m^T the iterative update scheme can be written like this [7]:

$$u^{(k,m)} = u^{(k-1,m)} + \alpha^{(k)} \frac{b_m - a_m^T u^{(k-1,m)}}{\|a_m\|_2^2} a_m \quad m = 1, 2, \dots, M, \quad k = 1, \dots \quad (2.8)$$

Here \cdot^T denotes the transpose and α is a parameter of the method called the relaxation parameter. This parameter could either be constant or change for each iteration, hence the $\cdot^{(k)}$ notation.

The SIRT method steps through all of the rows simultaneously, hence the name, and the update scheme can be written as such [7]

$$u^{(k)} = u^{(k-1)} + \alpha^{(k)} T_1 A^T T_2 (b - Au^{(k-1)}). \quad (2.9)$$

¹The system matrix A could be build using the AIRtools package [7]. In this project a modified version of, `paralleltomo.m` from AIRtools function, called `parbeam.m`, is used. This function was given to me by my supervisor Jakob Sauer Jørgensen.

Here T_1 and T_2 are symmetric positive matrices that defines different types of SIRT methods. Two common versions are the Landweber and Cimmino methods [9]. For the Landweber method both matrices are the identity matrix $T_1 = T_2 = \mathcal{I}$. For the Cimmino method $T_1 = \mathcal{I}$ and T_2 is a diagonal matrix with elements $\frac{1}{M} \frac{1}{\|a_m\|_2^2}$.

The advantages for discrete model is that they model the geometry of the scanning set-up better than the analytical methods [10]. So for scanning set-ups with restricted data, where it for example only is possible to scan in a limited range of angles, or where we can only acquire a certain number projections for each angle, the iterative methods have a clear advantage.

Most of the commercial CT scanners use filtered back projection [11], even though these iterative methods have existed in the literature for more than 40 years [8] and have been tested for many years as well.

In Figure 2.9 an comparison of FBP and IR with limited data is shown. In this example the artefacts inside the object makes it harder to see some of the smaller objects on the FBP solution, though the IR solutions are a bit blurred. The AIRtools package [7] has been used to produce these results.

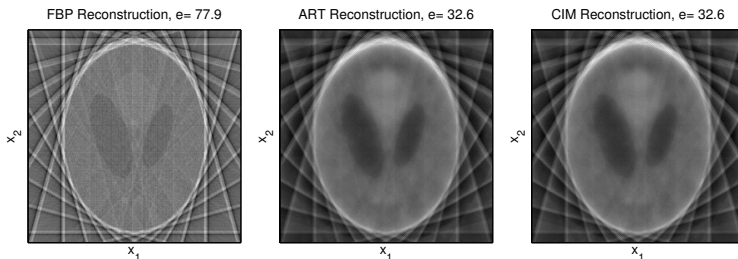


Figure 2.9: 2D Shepp-Logan phantom example of limited data, where only 12 evenly distributed angles are chosen for $\theta \in [0^\circ, 179^\circ]$, to show the advantage of the IR methods. The ART method has iterated for 10 iterations, with $\alpha = 0.25$, and the slower converging Cimmino method for 50 iterations with $\alpha = 1/\sigma_1^2$, for σ_1 being the largest singular value of $A^T T_2 A$.

The biggest disadvantage of the IR methods is that they are relatively slow, in a computational sense, due to the fact that one single iteration requires essentially both a forward projection and a backward projection [10]. Dependent on which iterative algorithm is chosen and how difficult the problem is, convergence of the algorithm to a good result could require many iterations, which clearly makes IR computationally slow, when comparing to FBP.

Another disadvantage, related to this, is the lack of a distinct stopping criterion, which is a problem because these methods do not necessarily converge

toward the solution we perceive as the best solution. So some useful stopping criterion is needed in order to stop iterating when the best solution is reached.

These disadvantages could be the reason that iterative methods are not used in commercial CT scanners. However a method such as ART which operates row-by-row, could actually start calculating on the first iteration sweep before all measurements were taken, which along with other initiatives, could help speeding up the IR method. More details on the use of iterative methods in commercial CT can be found in [11].

2.1.3 Regularization

The linear system matrix A from (2.7) is often ill-conditioned, meaning that the condition number is high and that inversion of this will give numerical inaccuracies. This is especially a problem when the measurements are affected by measurement noise, since these inaccuracies could end up amplifying the noise drastically and thus distorting the solution. Just as the modified filtering for the FBP method, we need to handle the noise when using the discrete model. This can be done by regularizing the solution, such that we force it to behave in an expected way. Here it should be noted that introducing regularization is the task of imposing some prior knowledge of the object of interest.

When introducing regularization we lose the iterative formulations from the previous section, since we cannot include regularization in the update functions (2.8) and (2.9). Instead we set up a optimization problem formulation which allows us to introduce the regularization term. This formulation is still based on the discrete linear formulation (2.7) and since we still wish to fit the reconstruction u to measurements b , we want projected image Au to be as close to b in some sense. The difference between Au and b is often measured in some norm $\|\cdot\|$ and this is called the data fidelity term $T(u) = \|Au - b\|$, which is the first of the two term of the regularization formulation. The other term, which is not related to the linear model, is the regularizer $R(u)$. The regularization formulation can be written as:

$$u_\alpha^* = \underset{u}{\operatorname{argmin}} \{T(u) + \alpha R(u)\}.$$

Where $\alpha \in \mathbb{R}^+$ is a regularization parameter. For $T(u) = \|Au - b\|_2^2$ and $\alpha = 0$ this becomes the least squares problem.

The introduction of this regularization formulation opens a wide variety methods since there is a choice of the two terms $T(u)$ and $R(u)$, a choice of op-

timization method and a choice of the parameter α . The choice of optimization method will not be discussed in this project, only mentioned, since it can be an entire research topic in itself. The choice of α will be slightly discussed in the following and the choice of the two terms will be elaborated in more detail.

There are several ways to choose the "best" value for the parameter α , it could be based on the relationship between $T(u^*)$ and $R(u^*)$, it could be based on a statistical method using for example cross-correlation or some other way of determining α . This depends on several things, especially how the "best" value is determined. An overview of some of the methods can be found in chapter 5 of [9].

A highly considered regularization method is the so called Tikhonov regularization method. For this method the two terms are $T(u) = \|Au - b\|_2^2$ and $R(u) = \|Du\|_2^2$, where D is a matrix, it could be the identity matrix or a finite difference approximation of a derivative operator. For D being the identity, a minimization of the regularized formulation forces the solution u to be as small as possible, where larger values are penalized the most, which will decrease the solution values, dependent on α . For D being a finite difference matrix minimization of the regularized formulation would minimize differences between neighbouring pixels such that the solution would become more smooth.

$T(u) = \|Au - b\|_2^2$ is not necessarily the best suited norm for the reconstruction problem, but within this project that is the data fidelity term which is considered. When considering the best suited data fidelity term both the noise and the specific reconstruction problem among other things, can be to account, which makes this a complex task.

When choosing the regularizing term $R(u)$ it is very problem dependent which term will give the best results. Therefore prior knowledge of the problem and object, that is some general expected tendencies which can be formulated mathematically, will be a good starting point for choosing this term. It has been shown that Total Variation (TV) can be advantageous prior for reconstruction problems with piecewise constant element [6],[2]. Since objects that are analysed with X-rays often are piecewise constant this prior seem like a reasonable prior to introduce. The theory behind TV is elaborated upon in the following.

Total Variation

The Total Variation (TV) approach to regularization is based on objects which are expected to be piecewise constant. For reconstruction problems this prior knowledge seem reasonable, since the objects we reconstruct is expected to be separated into components with different properties, whether it is hard tissue, soft tissue or both.

In the continuous setting where a 2D object can be described by a continuous function $f(x_1, x_2)$ over some domain Ω . The TV of f can be expressed by the following operator

$$J_{TV}f = \int_{\Omega} \sqrt{\left(\frac{\partial f}{\partial x_1}\right)^2 + \left(\frac{\partial f}{\partial x_2}\right)^2} dx_1 dx_2.$$

For this to fit as an expression for the regularizer term, this has to be discretized. The corresponding discrete formulation of the total variation can be expressed as such:

$$R_{TV}(u) = \sum_{n=1}^{N^2} \|D_n u\|_2,$$

where n is the pixel-index, D_n is the local derivative of pixel n and N^2 is the total number of pixels. The data fidelity term used for this method is the squared 2-norm.

An optimization algorithm solving the TV regularization problem has been implemented in MATLAB. This algorithm and the implementation is presented in further details in [chapter 6](#).

2.1.4 Measurement noise

When measuring the X-rays at the detector some noise will inevitably affect the collected data. This noise is often modelled as normally distributed noise, but by considering the data acquisition we introduce a more realistic noise model. The X-ray detector counts the number photons that arrives at it, so knowledge of the photon count can be used to simulate more realistic Poisson distributed noise.

The number of expected photons transmitted by a X-ray source can be approximated by a Poisson distribution [1] and so can the number of detected photons. In practice the Poisson distributed noise can be simulated by modifying the simulated measurements using a random Poisson distribution and an estimate of the number of detected photons.

2.2 Summary

Computed tomography has been presented with formulations of a continuous and a discrete model. Different reconstruction methods for both the continuous and discrete model are presented with some examples of reconstruction results. Regularization and especially Total variation is introduced and finally measurement noise is also introduced.

When measurement data is affected by noise, absorption based tomography, as it has been presented in this section, can still give some problems even if regularization techniques are used. This could for example be when objects with low absorption are examined, or when components in an object is desired to be distinguishable, but have very similar absorption properties. For these cases the different data handling techniques, such as either filtering or regularization, will not be enough to give good results. Therefore a different data acquisition technique is needed.

CHAPTER 3

PHASE CONTRAST FORWARD MODEL

The physical background behind Phase contrast imaging is presented with a short introduction to the different phase contrast techniques. The technique in focus for this project, free space propagation, is presented in further details with advantages and limitations. Experimental settings and mathematical derivations of a model for free space propagation is presented. As such the forward model of phase contrast tomography is presented and finally examples from an implementation of this is presented.

Phase contrast imaging covers a wide variety of X-ray tomography methods related to methods presented in [chapter 2](#) especially in [section 2.1](#). Phase contrast tomography utilizes the fact that electromagnetic waves, for example X-rays, are not only attenuated when interacting with matter, but the phase of the wave is also shifted [\[5\]](#).

Some of the advantages of using phase contrast as opposed to absorption based tomography can be:

- Small differences in material samples can be detected.
- Material distinction in object with different parts of very similar refractive properties.
- Especially better for higher energy beams in some materials, as seen for aluminium in [Figure 3.1](#) where the phase effect is higher than than the amplitude effect.

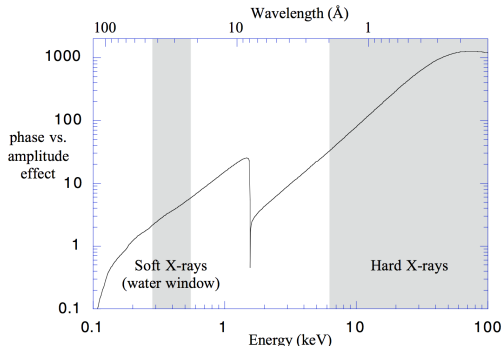


Figure 3.1: Ratio of the effect on the phase and the amplitude of a transmitted wave as a function of the X-ray energy for the element aluminium. Taken from [12].

3.1 Phase contrast

Electromagnetic waves such as X-rays are usually modelled by the electromagnetic wave equation which comes from Maxwell's equations. These waves have components of both an electric and a magnetic field. Here it is assumed that the X-ray waves are plane waves, such that they follow $\exp(i\frac{2\pi}{\lambda}nd)$ after interaction with an object [12], where i is the imaginary unit, d is the thickness of the object and n_i is the refractive index of the object. Normally the refractive index is just an index number describing the speed of the X-rays in vacuum and in a medium or an object. When the interaction with the object describes both an attenuation and a refraction of the X-ray wave, the refractive index can be modelled as a complex index, in order to include both. The complex refractive index of materials n_i can be described by the two components, the refractive index decrement, δ , and the absorption index, β :

$$n_i = 1 - \delta + i\beta$$

Here β should not be confused with the absorption/attenuation *coefficient* often denoted μ , which is proportional to the index through $\mu = \frac{4\pi}{\lambda}\beta$, where λ is the X-ray wavelength [13]. The effects of δ are related to the so-called Thomson scattering and the effects of β are related to the photoelectric effect and inelastic Compton scattering [14]. So where β attenuates the amplitude of the X-ray waves, the refractive index δ changes the phase of the waves, such that they are shifted relative to each other, this is called the phase shift. The relation shown in Figure 3.1 is the relation between δ and β which is seen to increase for higher energy X-rays.

For absorption based tomographic methods the phase shift caused by the refractive index decrement in the material is so small, that the effect of this refraction is negligible when the intensity is measured at a relatively short distance after the wave has exited the object. But further away from the object this phase shift is detectable. Combining the complex refraction index with the plane wave exponential function we get an expression which describes the attenuation and phase shift the X-ray waves:

$$\exp\left(i\frac{2\pi}{\lambda}n_id\right) = \exp\left(-\frac{2\pi}{\lambda}\beta d\right) \cdot \exp\left(i\frac{2\pi}{\lambda}(1-\delta)d\right). \quad (3.1)$$

This shows the attenuating effect of β in the decaying exponential function and phase shifting effect of δ in the complex exponential function.

The first two objectives, in order get data where this refractive information contained, is then to have: X-ray waves produced suited for the purpose and some specific data acquisition technique. As mentioned above there are a series of techniques which can be used for phase contrast tomography and these are also related to how the X-ray waves are produced. Some of the most well-known phase contrast techniques are listed below [3]:

- crystal interferometry,
- diffraction enhanced,
- Talbot interferometry,
- aperture-based,
- propagation-based.

Here the first two techniques use crystals and the optical properties of these. The next two use gratings with slits that in the right set-up can be used to find the phase contrast. The last method, which is the method we will focus on for this project, does not need either crystals or gratings. For propagation based phase contrast tomography, also called free space propagation, the experimental set-up is very similar to absorption based tomography where no optical components are needed, only an X-ray source and a detector.

The different methods presented above places different requirements on the X-ray source, though in common for all of them is the need for a parallel beam geometry as presented in [chapter 2](#) and shown in [Figure 2.2](#).

The energy of the X-ray waves should also be *quasi-monochromatic*, that is only consisting of waves with energies within a narrow energy band, which can

be achieved by filtering the waves. However there is a trade-off when filtering, since this will reduce the *brilliance* of the source and a high brilliance is also needed. So the source should have brilliance high enough that a filtering will not reduce this to much. The brilliance of the source is a way to measure the quality of the X-ray source, which depends on the photons emitted per second, the angular divergence of the rays, the area of the rays and the relative bandwidth of the monochromator crystal relative to 0.1% bandwidth [5]. Besides that, the methods also has a demand for high *transverse coherency* of the source. The coherency of the source is related to how the X-ray waves from the source behaves compared to each other. A way to quantify the coherency of the X-ray waves, is to calculate the cross-correlation between the spacial points on the waves, high cross-correlation then means that the waves emitted from the source travels similarly. Having Quasi-monochromatic waves is a necessary condition for having coherent waves.

Previously it was hard to achieve both high brilliance and coherency on any equipment besides the large synchrotron facilities. Today it is possible to produce laboratory equipment which is more suited toward delivering this, which has given new possibilities for the applications of phase contrast tomography. At the DTU physics department an experimental laboratory set up is being built, to carry out phase contrast tomography experiments. This project serves as an examination of the reconstruction methods related to phase contrast tomography that could be used for such an experimental set up.

For the free space propagation method there is also a demand for the resolution of the detector which should be a high resolution detector (for example with resolution of μm pixels). More on the physical model of the free space propagation in the following section, that is the *forward model* which the X-ray waves are assumed to follow.

3.2 Free space propagation

The idea behind free space propagation is mainly that if you move the detector in the direction of X-rays, such that there is some distance R between the object and the detector, the waves will propagate which will magnify the effects of the refraction. Propagation is the movement of electromagnetic waves in a medium, the propagation of X-rays is described in further details below.

As for standard CT, the idea in phase contrast tomography is to scan the object from different angles and so collect a sinogram of projections. A single linear projection of the refractive index and the absorption index in the direction

x_3 can be written like as [13]

$$B(\mathbf{x}) = \frac{2\pi}{\lambda} \int \beta(x_1, x_2, x_3) dx_3$$

$$\phi(\mathbf{x}) = -\frac{2\pi}{\lambda} \int \delta(x_1, x_2, x_3) dx_3$$

Here \mathbf{x} is a 2D Cartesian coordinate vector, B is the absorption image and ϕ the phase shift image. B and ϕ is not what we can measure on the detector, but the results of the wave interaction with the object.

A sketch to show the set up for free-space propagation PCT as opposed to purely absorption based tomography (ABT) is shown in [Figure 3.2](#).

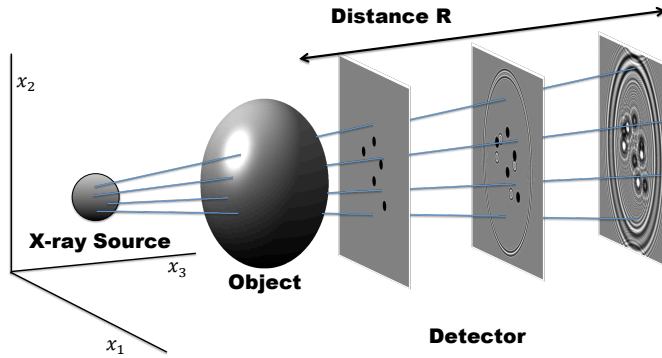


Figure 3.2: 3D sketch to show the difference in data acquisition between ABT and PCT. The 2D intensity images shown here are projections of a 3D object along the x_3 direction. The object here is a 3D ellipsoid, which is mainly weakly absorbing. Nine cylinders, which are projected to circles, lies along the x_3 direction inside the object. Five are either purely absorbing (black), four purely refracting (white) and the outer shell of the ellipsoid is also purely refracting. For the PCT method called free space propagation the experimental set up is similar to ABT. When the detector is close to object, $R \sim 0$, only the absorption B is detected, where further down, effects of both B and phase shift ϕ are detected.

The effects of the interaction with the object creates the transmission described by (3.1). Inserting the expressions for the phase shift and projected attenuation this becomes the Transmittance function T ,

$$T(\mathbf{x}) = \exp(-B(\mathbf{x})) \cdot \exp(i\phi(\mathbf{x})) \quad (3.2)$$

The transmittance $T(\mathbf{x})$ models the interaction of the X-rays with the object.

After passing the object, the X-rays propagate through the air. The behaviour of this propagation depends on the distance from the object R and also on the wavelength of the X-rays λ . The size of the smallest detectable elements q determines which regime that describes the propagation best. A way to understand why q is part of the relation, is that differences in the object acts as little slits, which causes diffraction patterns of the propagating wave. The width of these slits, that is q , is then the smallest detectable difference. So there are regions in which the propagation is modelled differently. A common way to separate these regions are as [5]:

$$\begin{aligned} \text{Contact region:} \quad R &\ll \frac{q^2}{\lambda} \\ \text{Fresnel region:} \quad R &\approx \frac{q^2}{\lambda} \\ \text{Fraunhofer region:} \quad R &\gg \frac{q^2}{\lambda} \end{aligned}$$

The Fresnel region is also known as the near field region and the Fraunhofer region as the far field region. The region which is most interesting for phase contrast tomography is the Fresnel region, since in this region the measured intensity contains information of both the attenuation and the phase shift. An example of the measurable intensity in these different regions are shown in Figure 3.3.

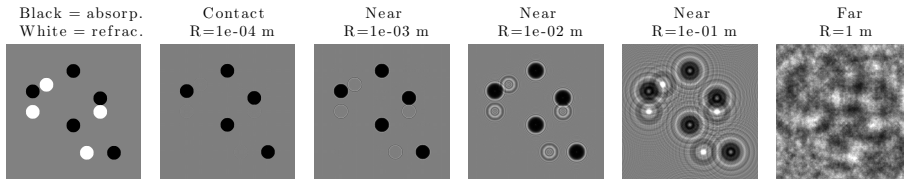


Figure 3.3: Simulations of detectable intensity through objects that are only absorbing and only refracting the X-rays, shown from several distances to show what information is "visible" in the intensity. This simulates 2D projections along the direction of the X-rays of a nine 3D cylinders which lies in the same direction. Wavelength $\lambda = 1\text{\AA}$, pixel size $0.1\mu\text{m}$ and diameter of circles $0.5\mu\text{m}$. Inspired by figure 9.2 in [5].

In the Fresnel region the propagation follows the Fresnel propagator given as a propagation function [13]:

$$P^R(\mathbf{x}) = -\frac{i}{\lambda R} \exp\left(\frac{i\pi}{\lambda R}|\mathbf{x}|^2\right)$$

By combining the transmission and the propagation a model for the intensity I can be expressed using the convolution operator \star as such [13]:

$$I^R(\mathbf{x}) = |T(\mathbf{x}) \star P^R(\mathbf{x})|^2$$

So the intensity is the squared modulus of the convolution of the transmitted X-rays with the Fresnel propagator. This intensity $I^R(\mathbf{x})$ is what is shown in both [Figure 3.3](#) and [Figure 3.2](#). For some applications presented in [chapter 4](#) the Fourier transform formulation is more desirable since the convolution is a product in Fourier space. By Fourier transform, formulated as in (2.4), denoted as $\hat{\cdot}$, the Fresnel propagator in Fourier space becomes:

$$\hat{P}^R(\boldsymbol{\omega}) = \exp(-i\pi R|\boldsymbol{\omega}|^2). \quad (3.3)$$

where $\boldsymbol{\omega}$ are the spatial frequencies. For a system where the resolution of the detector is known, the 2D spatial frequencies $\boldsymbol{\omega} = (\omega_1, \omega_2)$ are limited for discrete data. For p being the resolution, i.e. size of a pixel in meter (m) such that the sampling distance is $F_s = 1/p$, the discrete spatial frequencies are found in:

$$(\omega_1, \omega_2) \in \left[-\frac{F_s}{2}, \frac{F_s}{2} \right] \times \left[-\frac{F_s}{2}, \frac{F_s}{2} \right] \quad (3.4)$$

The free space propagation forward model describing the data acquisition from X-ray source to the recordable intensity has been presented. To set this in context of the inverse problem presented in [Figure 2.1](#) this intensity model is attempt to model the physical phenomena caused by the X-ray interaction. The unknown variables which describe the material components of the object are δ and β , and the intensities are the measurements. The intensity depends on the following parameters which are expected to be known for a specific experimental set up:

- Energy of the X-rays (assumed to be monochromatic) E , which determines the wavelength λ of the X-rays.
- Pixel size on the detector p_s
- Distance from object to detector R

And for this to follow Fresnel propagation as desired, these parameters should fulfil the Fresnel regime such that:

$$R \approx \frac{p_s^2}{\lambda} = \frac{E \cdot p_s^2}{c \cdot h},$$

where c is the speed of light in vacuum and h is Planck's constant.

For some of the solution methods presented in [chapter 4](#) measurements from several distances will be needed. From a data acquisition point of view this could be problematic since this can introduce some measuring errors such as misalignments of the measurements. Besides this, the data acquisition time will also be increased significantly when measurements has to be done from several distances.

3.3 Discretization and examples in 2D

In the previous section a forward model simulating the free space propagation of X-rays in the Fresnel regime is presented. In this section the forward model is discretized, but for the sake of simplification the forward model is formulated in a 2D setting instead of 3D. This way the derived discretized model from [section 2.1](#) can be used. When combining the forward model with tomography, multiple projections are recorded from different angles which are collected in a sinogram. Notation and some examples of tomographic measurements are simulated below.

The tomographic measurements are taken at different angles and for linear translations perpendicular to the direction of the X-rays similar to the technique for absorption based tomography. The notation is the same as in [section 2.1](#), such that the coordinate system of the scanner is rotated around the the coordinate system of the object. In this way several absorption images are collected into a sinogram holding the absorption data $B_\theta(t)$, and similarly for the phase shift data $\phi_\theta(t)$. Using the Radon transform these two sinograms can be written like this:

$$B_\theta(t) = \frac{2\pi}{\lambda} \int_{-\infty}^{\infty} \int_{-\infty}^{\infty} \beta(x_1, x_2) \cdot \delta_{\text{Dirac}}(t - x_1 \cos(\theta) - x_2 \sin(\theta)) dx_1 dx_2$$

$$\phi_\theta(t) = -\frac{2\pi}{\lambda} \int_{-\infty}^{\infty} \int_{-\infty}^{\infty} \delta(x_1, x_2) \cdot \delta_{\text{Dirac}}(t - x_1 \cos(\theta) - x_2 \sin(\theta)) dx_1 dx_2.$$

Where the new variable pair (θ, t) is the angle of rotation and t is the linear translation perpendicular to the direction of the X-rays. So this gives us the absorption and phase shift data from the absorption index and the refractive index decrement. The discretized formulation of this is similar to the one introduced in [section 2.1](#), where the object is separated into $N \times N$ pixels and the pixel expansion (2.6) is used. A single index notation is introduced $n = i + (N - 1)j$ for $i, j = 1, 2, \dots, N$, so $n = 1, 2, \dots, N^2$ and the absorption index and the refractive index decrement are collected in two column vectors, β_v and δ_v , with element index n . Using this expansion and discretization the discrete model from absorption and refractive index to absorption and phase shift data can be formulated as such:

$$B_v = A \left(\frac{2\pi}{\lambda} \beta_v \right)$$

$$\phi_v = A \left(-\frac{2\pi}{\lambda} \delta_v \right)$$

Here A is the matrix from (2.7) describing the length of the X-rays through each pixel. Column vectors B_v and ϕ_v holds discrete absorption and phase

shift data of $B_\theta(t)$ and $\phi_\theta(t)$. For N_θ and N_t begin the total number of angles and translations, respectively, the discretization for $B_{\theta_i}(t_j)$ becomes element $n = i + N_t(j - 1)$ in B_v , where $i = 1, 2, \dots, N_\theta$ and $j = 1, 2, \dots, N_t$. The length of these data vectors becomes $N_\theta \cdot N_t$. The reconstruction problem that has to be solved becomes two separate inverse problems:

We want to reconstruct

- absorption index β_v from absorption data B_v , and
- refractive index decrement δ_v from phase shift data ϕ_v .

With the knowledge the absorption and phase shift data, B_v and ϕ_v , it is clear now that the problem to be solved are two similar reconstruction problems, as considered in [subsection 2.1.2](#) and [subsection 2.1.3](#). However what is recorded at the detector are not these two sinograms, it is the combined intensity sinogram which is modelled by the transmission and propagation as described in [section 3.2](#). The intensity data which can be recorded at the detector is denoted as such:

$$I_\theta^R(t) = |T_\theta(t) \star P^R(t)|^2 \quad (3.5)$$

$$, \text{ where: } T_\theta(t) = \exp(-B_\theta(t)) \cdot \exp(i\phi_\theta(t)).$$

The discrete formulation of the intensity data I_v can be written using discrete notation introduced above. First the discrete transmission is introduced:

$$T_v = \exp(-B_v + i\phi_v).$$

Where \exp operates element-wise on the vectors. Since the projections of the 2D object are 1D, with variation along translation variable t , and the propagation function $P^R(t)$ is only varies in this dimension, the discrete propagation function is the same of any fixed angle θ_i . A column vector P_v^R is introduced that has the length $N_\theta \cdot N_t$ and is the propagation function evaluated at the same discrete points as B_v and ϕ_v . Based on this the discrete intensity data I_v^R becomes:

$$I_v^R = |T_v \star P_v^R|^2$$

Where $|\cdot|^2$ denotes an element-wise modulus squared operation and \star denotes a discrete convolution here. In practice this discrete convolution operation can be done by using the fact that a product in Fourier space is a convolution in real space. By using a 1D discrete fast Fourier transform (FFT) on T_v , in the direction where t varies, using the propagation function in the Fourier space [\(3.3\)](#) and finally using a 1D inverse FFT on the product of these, the discrete convolution is calculated. This method is used in the forward model implementation for this project.

To simulate this forward model, the discrete formulation above has been implemented and an example from absorption index and refractive index decrement, to the corresponding absorption and phase shift data, and finally to the intensity data is shown in [Figure 3.4](#) and [Figure 3.5](#).

The phantom used for these examples simulates a grain structure which consist of different materials. Since this phantom is used several times for this project it is explained in further details in [subsection 3.3.1](#).

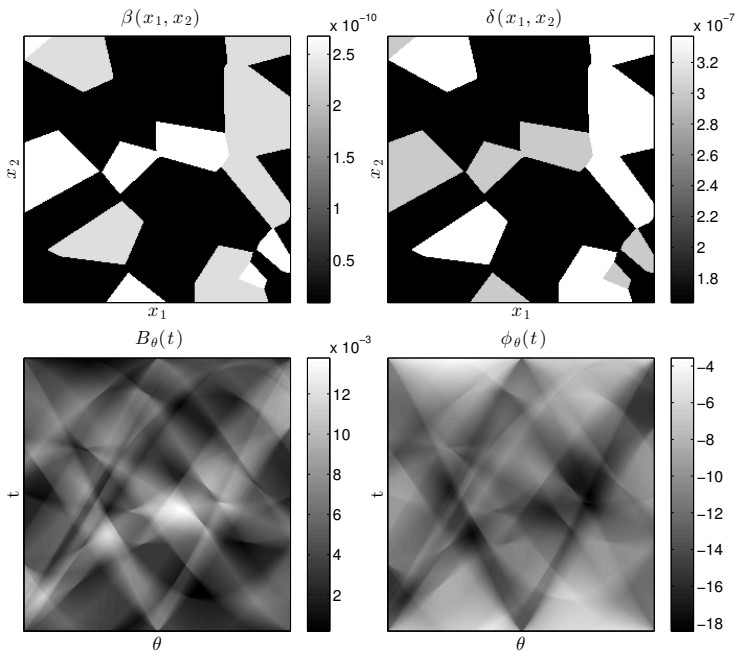


Figure 3.4: 2D slice example of forward simulation with grain phantom of with silicon and aluminium grains in a polycarbonate block. On the top original phantom and below the absorption and phase shift data. The absorption and phase shift data are not the sinograms which we are able to measure, but sinograms we want to find, in order to reconstruct β and δ . The original phantom sizes was $[256 \times 256]$ pixel. Tomographic settings here was 359 angles θ in $[0^\circ, 179^\circ]$ and 368 translations t for each angle.

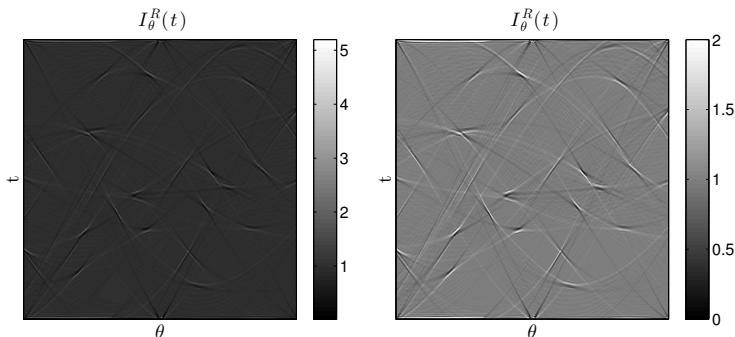


Figure 3.5: 2D slice example to show a forward simulation of the propagation of the absorption and phase shift data which gives the intensity measurements needed to make phase contrast tomographic reconstructions. This is what we can measure at the detector. Only one intensity sinogram is recorded at the detector, the two visualizations here are just shown in different color ranges, to visualize the structure better. The left sinogram has an actual linear colorbar and on the right sinogram all values above 2 has been truncated to color-value 2. In this simulation the X-ray energy was 40 keV, the distance from the object to the detector was $R = 0.5\text{m}$ and the pixelsize was $1\mu\text{m}$. Tomographic settings here was 359 angles θ in $[0^\circ, 179^\circ]$ and 368 translations t for each angle.

3.3.1 Phantom

The grain phantom, used for the example in [Figure 3.5](#), simulates a grain structure in a 2D slice object. The grains are constructed by making a series of Voronoi cells, which are a region of closest points to a series of random distributed centres ¹. The Voronoi cells are separated into three regions, 3/5 of the cells as "background", 1/5 of the cells as one material and the last 1/5 as another materials. For some of the examples the background will be a low absorbing material, for example polycarbonate as in [Figure 3.5](#). The two other materials will be chosen as higher absorbing materials, for example two sort of metal. In [Figure 3.5](#) the two metals chosen are silicon and aluminium, which are next to each other in the periodic table, and have very similar absorption and refraction properties. In [Table 3.1](#) the indexes for some materials are listed.

This phantom simulates a grain structure similar to what can be seen in physical materials science experiments. A good CT solution for this phantom is a solution where the distinction between the two materials and the background is clear and also the determination of what the materials are. The grains of

¹A implementation of function `phantomgallery.m`, which, among other thing, can be used to create these Voronoi cells, was given to me by my supervisor Per Christian Hansen

different materials are in several cases next to each other, which makes the distinction between them more difficult and such the different grains have different degrees of complexity, in the sense of a reconstruction problem.

Material	absorption index (β)	refractive index decrement (δ)
Polycarbonate($C_{16}H_{14}O_3$)	$8.43 \cdot 10^{-12}$	$1.64 \cdot 10^{-7}$
Carbon(diamond)	$1.90 \cdot 10^{-11}$	$4.55 \cdot 10^{-7}$
Magnesium	$1.15 \cdot 10^{-10}$	$2.22 \cdot 10^{-7}$
Aluminium	$2.32 \cdot 10^{-10}$	$3.37 \cdot 10^{-7}$
Silicon	$2.68 \cdot 10^{-10}$	$3.01 \cdot 10^{-7}$
Iron	$6.42 \cdot 10^{-9}$	$9.54 \cdot 10^{-7}$
Copper	$9.96 \cdot 10^{-9}$	$1.06 \cdot 10^{-6}$

Table 3.1: Absorption index and refractive index decrement for X-rays of energy 40 keV for different materials, taken from [15].

3.4 Summary

The two steps in the forward model of the free space propagation technique from the object to the measurements has been presented. The mathematical model is presented and an example of data produced by the forward model is presented. When we want to go back from the measurements to the original object, we have to go through these same two steps in the reverse order as illustrated in [Figure 3.6](#).

The reconstruction process in [Figure 3.6](#) is the same as for absorption based CT, so the techniques presented in [section 2.1](#) can be used for this. The *phase retrieval* process has not yet been presented, but the idea is go back from the propagated measurements (3.5) to the projected data. This process has been attempted in wide variety of ways, which will be presented in the next chapter about phase retrieval.

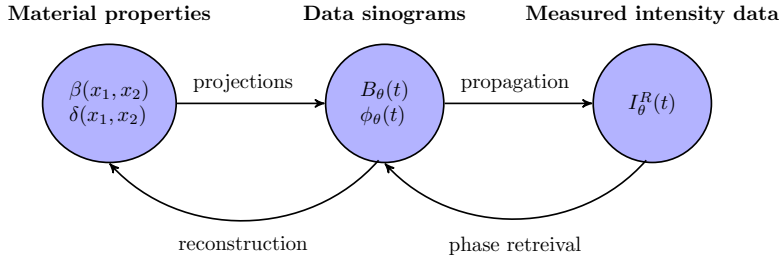


Figure 3.6: Diagram of the forward and inverse problems of phase contrast tomography, which shows the different stages from object to measurements. The absorption index β and refractive index decrement δ , in Cartesian coordinates (x_1, x_2) , are projected to the two sinograms: absorption data B and the phase shift data ϕ for angles θ and translations t . These two sinograms are not measurable, but just an intermediate step in the forward model. After the object, the X-ray waves are transmitted and propagated through the air to the detector where they are measured as the intensity I , a sinogram. Together these two parts are the forward model. To go back through the same two steps, the absorption and phase shift data are found through phase retrieval and finally the absorption index β and refractive index decrement δ can be found through a reconstruction.

PHASE RETRIEVAL

Phase retrieval for free space propagation, the task of calculating the absorption and phase shift data from intensity measurements, is presented. The focus is a linear phase retrieval method called the contrast transfer function. This method is derived mathematically based on a Taylor expansion of the transmission function. Besides this a simpler variant of the linear models, the duality method, is presented.

Phase retrieval in this setting is the task of calculating the phase shift and absorption from intensity measurements. Phase retrieval can be the task of other phase contrast techniques than free space propagation, though since the data and the forward problem are different, the phase retrieval technique for these methods also varies. So the phase retrieval methods presented here are related to and derived from the free space propagation method presented in [section 3.2](#). Besides this, the methods presented here are *linear* phase retrieval methods. The linear models are chosen since they have produced good results [\[13\]](#) and especially since a linear model is used when a combined phase retrieval and reconstruction method is examined in [chapter 5](#).

These phase retrieval methods are based on the intensity, which is the squared modulus of the transmitted electromagnetic wave convolved with a Fresnel propagator. The methods are linear with respect to $B_\theta(t)$ and $\phi_\theta(t)$ which can be achieved by a Taylor expansion, as described further below. Here the focus has been on one method, namely the contrast transfer function (CTF).

4.1 Phase retrieval methods

The phase retrieval method examined here is only linear in the Fourier domain, therefore the intensity is first rewritten in Fourier domain. Here the notation is similar to the notation from [section 3.2](#) to make it less complicated, i.e. the derivations are related to a single projection, but also applicable for an entire sinogram.

In the following the Fourier transform, as defined in [\(2.4\)](#), is used repeatedly.

The intensity can be reformulated as such:

$$I_R(x) = |T(x) \star P_R(x)|^2 = (T(x) \star P_R(x)) \cdot (T^*(x) \star P_R^*(x))$$

where \cdot^* denotes the complex conjugate. Therefore the Fourier transform of the intensity can be formulated as (here the Fourier transform of P_R , [\(3.3\)](#), is used):

$$\begin{aligned} \widehat{I}_R(\boldsymbol{\omega}) &= \left(\widehat{T}(\boldsymbol{\omega}) \cdot \exp(-i\pi R|\boldsymbol{\omega}|^2) \right) \star \left(\widehat{T}^*(\boldsymbol{\omega}) \cdot \exp(i\pi R|\boldsymbol{\omega}|^2) \right) \\ &= \int \exp(-i\pi\lambda R|\boldsymbol{\omega} - \boldsymbol{\tau}|^2) \cdot \widehat{T}(\boldsymbol{\omega} - \boldsymbol{\tau}) \cdot \exp(i\pi\lambda R|\boldsymbol{\tau}|^2) \cdot \widehat{T}^*(-\boldsymbol{\tau}) \, d\boldsymbol{\tau} \\ &= \exp(-i\pi\lambda R|\boldsymbol{\omega}|^2) \int \exp(2i\pi\lambda R\boldsymbol{\omega}\boldsymbol{\tau}) \cdot \widehat{T}(\boldsymbol{\omega} - \boldsymbol{\tau}) \cdot \widehat{T}^*(-\boldsymbol{\tau}) \, d\boldsymbol{\tau} \end{aligned}$$

This expression can be rewritten to [\[13\]](#), [\[16\]](#):

$$\widehat{I}_R(\boldsymbol{\omega}) = \int T\left(\mathbf{x} - \frac{\lambda R\boldsymbol{\omega}}{2}\right) \cdot T^*\left(\mathbf{x} + \frac{\lambda R\boldsymbol{\omega}}{2}\right) \exp(-2\pi i\mathbf{x} \cdot \boldsymbol{\omega}) \, d\mathbf{x}. \quad (4.1)$$

Here the inverse Fourier transform of a convolution is used, as well as an assumption that the absorption is weak ($B(\mathbf{x}) \ll 1$) and the phase is slowly varying. This intensity formulation will then be the starting point for the derivation of the linear phase retrieval method.

4.1.1 The CTF method

For the contrast transfer function (CTF) the transmission $T(x)$ is linearized by Taylor expanding around

$$-B(\mathbf{x}) + i\phi(\mathbf{x}) = 0.$$

Using $g = -B(\mathbf{x}) + i\phi(\mathbf{x})$ and $g_0 = 0$ the Taylor expansion of the transmission function (3.2) becomes:

$$\begin{aligned} T(\mathbf{x}) &= \exp(g_0) + \exp(g_0)(g - g_0) + \mathcal{O}(g^2) \\ &= 1 + g + \mathcal{O}(g^2) \\ &= 1 - B(\mathbf{x}) + i\phi(\mathbf{x}) + \mathcal{O}\left(B(\mathbf{x})^2, \phi(\mathbf{x})^2, B(\mathbf{x}) \cdot \phi(\mathbf{x})\right) \end{aligned}$$

Neglecting the terms of order two or higher, we arrive at a linear approximation of the transmission $T(\mathbf{x}) \approx 1 - B(\mathbf{x}) + i\phi(\mathbf{x})$. This is inserted into (4.1) (here $k = \frac{\lambda R \boldsymbol{\omega}}{2}$ is used for simplicity):

$$\begin{aligned} \widehat{I}_R(\boldsymbol{\omega}) &\approx \int \left(1 - B(\mathbf{x} - k) + i\phi(\mathbf{x} - k)\right) \cdot \left(1 - B(\mathbf{x} + k) - i\phi(\mathbf{x} + k)\right) \\ &\quad \cdot \exp(-2\pi i \mathbf{x} \cdot \boldsymbol{\omega}) \, d\mathbf{x} \end{aligned}$$

In order to achieve a linear expression, terms of second order or higher are neglected, which leaves:

$$\begin{aligned} &\int \left(1 - B(\mathbf{x} - k) - i\phi(\mathbf{x} - k) - B(\mathbf{x} + k) + i\phi(\mathbf{x} + k)\right) \cdot \exp(-2\pi i \mathbf{x} \cdot \boldsymbol{\omega}) \, d\mathbf{x} \\ &= \delta_{\text{Dirac}}(\boldsymbol{\omega}) + \int \left(-B(\mathbf{x} - k) - i\phi(\mathbf{x} - k)\right) \cdot \exp(-2\pi i \mathbf{x} \cdot \boldsymbol{\omega}) \, d\mathbf{x} \\ &\quad + \int \left(-B(\mathbf{x} + k) + i\phi(\mathbf{x} + k)\right) \cdot \exp(-2\pi i \mathbf{x} \cdot \boldsymbol{\omega}) \, d\mathbf{x} \\ &= \delta_{\text{Dirac}}(\boldsymbol{\omega}) + \exp(i\pi\lambda R|\boldsymbol{\omega}|^2) (-\hat{B}(\boldsymbol{\omega}) - i\hat{\phi}(\boldsymbol{\omega})) \\ &\quad + \exp(-i\pi\lambda R|\boldsymbol{\omega}|^2) (-\hat{B}(\boldsymbol{\omega}) + i\hat{\phi}(\boldsymbol{\omega})) \\ &= \delta_{\text{Dirac}}(\boldsymbol{\omega}) - 2 \cos(i\pi\lambda R|\boldsymbol{\omega}|^2) \hat{B}(\boldsymbol{\omega}) + 2 \sin(i\pi\lambda R|\boldsymbol{\omega}|^2) \hat{\phi}(\boldsymbol{\omega}) \end{aligned}$$

Here integral variable substitution, Fourier transform and Euler's formula has been used, as well as k replaced by the original value $\frac{\lambda R \boldsymbol{\omega}}{2}$. A linear model in Fourier space has been derived which, based on intensity measurements, can be used for calculating $\hat{B}(\boldsymbol{\omega})$ and $\hat{\phi}(\boldsymbol{\omega})$ for known details of the experimental system, such as the wavelength λ , the distance from object to detector R and the resolution of the detector, which can be used to find the relevant spacial frequencies (3.4).

The most conspicuous about this model might be the fact that for each intensity measurement, there are two unknown to be found. This will give a highly underdetermined system, unless there are measurements multiple detector positions. For measurements from two distances there will be the same amount of measurement as variables, which can help to solve this problem. This is one

way to handle this problem of data to variables ratio, another is called the *duality* method, which is elaborated upon in [subsection 4.1.2](#). Measurements from even more than two distances will give more data and therefore this can be a way to produce even better results, which is the case in for example [\[13\]](#). However, as mentioned in [section 3.2](#), more than one distance can introduce some misalignments which will introduce systematic errors.

The function $\delta_{\text{Dirac}}(\omega)$ is the Dirac delta which comes from the constant 1. This could potentially result in a problem, since it becomes infinitely large for input 0. In order to avoid any problems with this, the zero-frequency should be handled separately. Other frequency problems arises when the cos or sin terms become 0, since this leaves the corresponding variables that we are solving for, to be chosen freely. This is called *zero-crossings* problems. When measuring from several distances this problem is reduced, since the zero crossings will be shifted because they are dependent on the distance parameters R , but for two distances this could be a problem.

The CTF method gives the best results for objects with low absorption [\[13\]](#), so this is an important disadvantage of this method. However some of the examples, where absorption based tomography can have problems and PCT could be useful, is exactly when the absorption is low.

To set the CTF method into the setting of the discrete 2D formulation presented in [section 3.3](#). The data from the forward model are the intensity measurements for example from two distances: $I_{\theta}^{R_1}(t)$ and $I_{\theta}^{R_2}(t)$. The real data is discrete so in the discrete notation the data becomes $I_v^{R_1}$ and $I_v^{R_2}$. The measured data is Fourier transformed, discretely, using FFT along the direction where t varies. The transformed data is then denoted as $\widehat{I}_v^{R_1}$ and $\widehat{I}_v^{R_2}$. In Fourier space the frequency domain is also discretized as described by [\(3.4\)](#), though since the projections are only 1D, the spacial frequencies only varies in this direction. The spacial frequencies are split into N_t , as for variable t , evenly spaced values, and since it is the same for each angle θ they are repeated every time θ changes. Single index notation of the spacial frequencies is denoted ω_n where $n = i + N_t(j - 1)$ and $i = 1, 2, \dots, N_t$ and $j = 1, 2, \dots, N\theta$. The linear system can be denoted by having the cosine and sine functions in two diagonal matrices C and S [\[3\]](#):

$$C(R) = \begin{pmatrix} \cos(i\pi\lambda R|\omega_1|^2) & 0 & \cdots & 0 \\ 0 & \cos(i\pi\lambda R|\omega_2|^2) & \cdots & 0 \\ \vdots & \vdots & \ddots & 0 \\ 0 & 0 & \cdots & \cos(i\pi\lambda R|\omega_K|^2) \end{pmatrix}$$

$$S(R) = \begin{pmatrix} \sin(i\pi\lambda R|\omega_1|^2) & 0 & \cdots & 0 \\ 0 & \sin(i\pi\lambda R|\omega_2|^2) & \cdots & 0 \\ \vdots & \vdots & \ddots & 0 \\ 0 & 0 & \cdots & \sin(i\pi\lambda R|\omega_K|^2) \end{pmatrix},$$

where $K = N_\theta \cdot N_t$ is the total number of frequencies. The unknowns, we are solving for, are the absorption data B_v and the phase shift data ϕ_v . These variables are Fourier transformed, discretely using FFT: \widehat{B}_v and $\widehat{\phi}_v$, in order to be able to set up the linear model. For the two distances, R_1 and R_2 , the linear model becomes:

$$\begin{pmatrix} \widehat{I}_v^{R_1} \\ \widehat{I}_v^{R_2} \end{pmatrix} = \underbrace{\begin{pmatrix} -2C(R_1) & 2S(R_1) \\ -2C(R_2) & 2S(R_2) \end{pmatrix}}_G \begin{pmatrix} \widehat{B}_v \\ \widehat{\phi}_v \end{pmatrix} \quad (4.2)$$

If several distances were measured, this would be introduced as new rows of in the matrix G by $C(R)$ and $S(R)$ again, and the measurements would be stacked on the left hand side. G is a very sparse matrix, since it is only built from diagonal matrices and in the case of two distances, it becomes a tridiagonal matrix. When implementing this method the model in G avoid zero-frequencies by only using frequencies that is close to 0, but not exactly 0. The zero-crossings problems are avoided by using a mask which marks the zero crossings and just assuming that the solution is zero at these crossings, since the solution here could be arbitrary according to the model.

The linear CTF phase retrieval method has been presented. To use it in practice, the measurements are first Fourier transformed. Next, the model relating the absorption and phase shift data to the intensity, in the Fourier space, is set up and solved. After this, the results are inversely Fourier transformed to achieve results in Cartesian coordinates in real space.

4.1.2 The duality method

The duality method is a way to simplify the linear phase retrieval methods, such that they only require measurements from a single distance. This is mainly desirable for two reasons; it will speed up the data acquisition time and it will reduce alignment and other errors introduced by measuring at two or more distances. The method is based on the assumption that the absorption and phase shift data are proportional. This assumption will not hold for all objects, but even for objects where this does not hold for all materials, this method has shown some good results [17]. A proportionality constant, σ , between the

absorption and phase shift data is introduced:

$$\sigma = \frac{\phi}{B} = -\frac{\delta}{\beta}$$

For some materials, such as for example the phantom with aluminium and magnesium from [section 3.3](#), this factor is not constant. However, for σ is chosen within a range of realistic values, this will not have a significant influence the results as also explained in [chapter 7](#).

Using the proportionality assumption with constant factor σ , the CTF method, formulated with respect to the absorption data, becomes:

$$\begin{aligned} \widehat{I}_R(\boldsymbol{\omega}) &\approx \delta_{\text{Dirac}}(\boldsymbol{\omega}) - 2 \cos(i\pi\lambda R|\boldsymbol{\omega}|^2)\widehat{B}(\boldsymbol{\omega}) + 2 \sin(i\pi\lambda R|\boldsymbol{\omega}|^2)\sigma\widehat{B}(\boldsymbol{\omega}) \\ &= \delta_{\text{Dirac}}(\boldsymbol{\omega}) + \left(2\sigma \sin(i\pi\lambda R|\boldsymbol{\omega}|^2) - 2 \cos(i\pi\lambda R|\boldsymbol{\omega}|^2)\right)\widehat{B}(\boldsymbol{\omega}) \end{aligned}$$

This leaves a linear correspondence between the measurements and the absorption data in the Fourier space, and using this model, phase retrieval can be carried out based on measurements from a single distance.

Writing up the discrete linear model for the Fourier transformed intensity data, as in [subsection 4.1.1](#), the linear problem for the CTF duality method is:

$$\widehat{I}_v^R = \underbrace{(-2C(R) + 2\sigma S(R))}_W \widehat{B}_v. \quad (4.3)$$

This is a linear model with a diagonal matrix, which means that it is very easy to solve, as long as the diagonal elements are non-zero.

4.2 Summary

Some phase retrieval techniques has been presented and derived. Using these methods the absorption and phase shift data can be found from intensity data measurements. When the projected data is retrieved from the measurements, then the next step is to go back and calculate the absorption index and refractive index decrement using one of the different reconstruction methods presented in [section 2.1](#).

PHASE CONTRAST TOMOGRAPHY

This chapter combines the three previous chapters by examining tomographic reconstructions from measurements of phase contrast data. The first part focuses on the two stage method, which is phase retrieval followed by reconstruction. Next the algebraic combined method is introduced, where the phase retrieval is combined with the reconstruction into one combined linear model, such that the reconstructions can be done in one step. Details of what and how the different methods are implemented and their differences is also presented.

In this chapter the phase contrast tomographic data, which now can be simulated, is run through the phase retrieval methods presented previously and finally the original object is reconstructed. In this way it becomes possible to simulate physical experiments with different materials, different retrieval methods, different reconstruction methods and different experimental set ups such as variable distance and energy among other things. The two main classes of PCT methods presented here are: 1) the two stage (TS) method, where the two stages are phase retrieval and reconstruction and 2) the algebraic combined (AC) method, where the phase retrieval and the reconstruction is combined into one step.

5.1 Two stage reconstruction method

The *two stage method* is the phase contrast tomography method which consists of a stage of phase retrieval which is followed by a stage of reconstruction as illustrated in [Figure 3.6](#). This two stage method is a classical way to retrieve the absorption index and refractive index decrement from intensity measurements. In other set ups in the literature the reconstruction methods used has been

Filtered Back Projection or Tikhonov regularization [13],[18]. For this project the focus is reconstructions using TV-regularization. Since TV-regularization has shown good results for normal absorption based CT [2] and also has been used for phase contrast tomography [3] we expect that it is a regularization method which will give good results for PCT problems.

The two stage method implemented within this project comes in two different versions dependant on the phase retrieval method:

- The first method is based on measurements from two different detector positions placed at distances R_1 and R_2 . For the phase retrieval stage the standard CTF method is used, where the system (4.2) is set up and solved with respect to discretely Fourier transformed absorption and phase shift data. This method is referred to as **TS2R**, short for two stage method with two R distances for the measurements.
- The second method is based on measurements from a single detector position placed at the distance R . This method uses the CTF duality method where an absorption and phase shift proportionality is assumed. In this version the system (4.3) is set up and solved with respect to the discretely Fourier transformed absorption data. This method is referred to as **TSD**, short for two stage method based on duality assumption.

For both methods the data is inversely Fourier transformed after solving the respective linear systems. For TS2R this results in both absorption and phase shift data, i.e. data for two reconstruction problems. For TSD the phase retrieval results in the absorption data, which is then the data for a single reconstruction problem. So this concludes the first stage of phase retrieval.

For the second stage, reconstruction, both TS2R and TSD uses Total Variation regularization. An optimization algorithm for solving the TV-problem has been implemented, which is used to solve the two reconstruction problems for TS2R and the one reconstruction problem for TSD. To make a fair comparison of the different tomography methods the same optimization method is used for the TV regularization for all methods. Since the same optimization method is used, the details of the method and implementation choices, are outlined in [chapter 6](#).

This concludes the two implemented versions of the two stage PCT method, and what the two stages consists of. These methods are now ready to be used in a the setting of simulated experiments.

5.2 Algebraic combined method

The idea of an algebraic combined (AC) method is to make one combined method as opposed to the two stage (TS) method presented in [section 5.1](#). This idea has been examined before in different settings, for example in [\[18\]](#) where the combined method is based on filtered back projection reconstructions with 2D filters, or in [\[3\]](#) where a linear formulation is set up and reconstruction is done using TV-regularization. The setting for this project is similar to the formulation in [\[3\]](#), though the objective is also to compare the AC method to the two stage method presented in [section 5.1](#). This comparison is done in order to show advantages and disadvantages of having a combined model as opposed to a two stage model for simulated physical experiments. The models presented in this section are different from [\[3\]](#), since they are build on the discrete formulation detailed in [subsection 2.1.2](#). This discretization is the basis for formulating simulated experiments in correct physical units. In this way the methods from discretization to the modelling are done with correct physical units in mind.

The AC model should therefore combine the phase retrieval methods presented in [chapter 4](#) with the discrete reconstruction methods presented in [subsection 2.1.2](#) and [subsection 2.1.3](#). Since the discrete model presented in [section 3.3](#) is linear in real space and both versions of the CTF method is linear in Fourier space, a Fourier transform is needed in order to combine these two methods linearly. The measurement data consists of 1D projection of a 2D object from different angles and the Fourier transform is then a discrete transform of each of the 1D projections. One way to handle this transform, is to make a combined operator \mathcal{FR} which combines the Fourier transform with the Radon transform such that $[\mathcal{FR}f](\omega_1, \omega_2) = \mathcal{F}(\mathcal{R}(f(x_1, x_2)))$. In the discrete formulation, the columns of system matrix A presented in [\(2.7\)](#) corresponds the different projections of each discrete pixel. By discretely Fourier transforming each these columns, only along translation variable t , a matrix \hat{A} can be created which describes the linear model from object to Fourier transformed sinogram. Using this discrete definition a discrete algebraic model, combing the phase retrieval and discrete linear model, can be formulated. Two version of the phase retrieval method CTF has been presented and therefore there will also be two versions of the AC method:

- The first method is, like the TS2R mehtod, based on measurements from two different detector positions placed at distances R_1 and R_2 . Using

matrix G from (4.2) and \widehat{A} the linear discrete AC2R model becomes:

$$\begin{pmatrix} \widehat{I}_v^{R_1} \\ \widehat{I}_v^{R_2} \end{pmatrix} = G \underbrace{\begin{pmatrix} \frac{2\pi}{\lambda} \widehat{A} & 0 \\ 0 & -\frac{2\pi}{\lambda} \widehat{A} \end{pmatrix}}_Q \begin{pmatrix} \beta_v \\ \delta_v \end{pmatrix}.$$

This model is based on Fourier transformed intensity data as marked with $\widehat{\cdot}$. Combining matrices G and Q this gives a linear model which relates the absorption index and the refractive index decrement to the Fourier transform of the measured intensity data. A function for setting up the linear model has been implemented, where the matrix combination of G and Q is calculated, based on the settings of a simulated or real experiment. With measurements from two distances a TV regularization problem can be defined, and the implemented optimization algorithm can be used to solve this. This version of the AC method is referred to as **AC2R**, short for algebraic combined method using two R distances for the measurements.

- The second version is based on a single detector distance, as for TSD, placed at the distance R . The phase retrieval step is based on the CTF duality method, which is based on an proportionality assumption between the absorption and phase shift. Combing the CTF duality model (4.3) and \widehat{A} the linear discrete ACD model can written up as such:

$$\widehat{I}_v^R = W \frac{2\pi}{\lambda} \widehat{A} \beta_v$$

The model here is based on the intensity data which is discretely Fourier transformed. A function for setting up the matrix V has been implemented, which is only based on the experimental settings of a simulated or real experiment. With data from a single distance measurement, a TV-regularization model can be set up and solved using the implemented optimization algorithm, which will give the absorption index of the object, proportional to the refractive index decrement δ with factor $-\sigma$. This version is referred to as **ACD**, short for algebraic combined method using the duality CTF phase retrieval method.

For the TS and ABT method the reconstruction problem, that has to be solved, is based on the system matrix A , which is a large, but sparse, matrix. Since this matrix is sparse this can stored and applied without using too much memory. For the AC method the matrix \widehat{A} is part of the system matrix and this makes the system matrix dense due to the Fourier transform. This means that storing it would demand a lot of memory, which can cause problems for a practical implementation. Instead of storing the system matrix, a matrix-free implementation

could be a solution to this problem. A matrix-free implementation is based on a function which can give the same result as applying, for example, the matrix A to a vector x , though without setting up the matrix A . This function can be much less memory demanding since a large dense matrix is avoided, though it could be computationally slower than applying a matrix multiplication. For the combined matrix \widehat{A} a matrix-free implementation would apply the matrix A first followed by a Fourier transform of the resulting sinogram.

For several optimization algorithms for TV-regularization the transpose of the system matrix is needed [19],[20]. In a matrix-free implementation, this means that a function for applying the transpose of a matrix, \mathcal{A}^T to a vector y also has to be implemented. If the system matrix consists of a combination of other matrices, as the case for the AC2R and ACD methods, the rule for transpose of matrices has to be used $((FR)^T = R^T F^T)$. For the combined matrix \widehat{A} , the transpose would correspond to applying the transpose of the Fourier transform first, followed by a transpose of the system matrix A . Since the Fourier transform is an orthonormal operator its inverse corresponds to its transpose. Therefore the transpose of the combined operator \widehat{A} consists of an inverse Fourier transform followed by matrix A^T , this is denoted as \widehat{A}^T . For the AC2R method the transposed system matrix becomes $Q^T G^T$ where Q^T is:

$$Q^T = \begin{pmatrix} \frac{2\pi}{\lambda} \widehat{A}^T & 0 \\ 0 & -\frac{2\pi}{\lambda} \widehat{A}^T \end{pmatrix}.$$

For the ACD method the transpose of the system matrix becomes $\frac{2\pi}{\lambda} \widehat{A}^T W^T$.

5.3 Summary

Four solution methods to the phase contrast tomographic problem, based on the free space method, has been presented. All of the methods uses the CTF phase retrieval technique. Two of them uses the phase retrieval and reconstruction in separate steps, the TS methods, and the other two, the AC methods, uses a combination of the phase retrieval and reconstruction in one step. The matrices needed in order to set up a TV-regularization formulation has been presented for all four methods, and next an optimization algorithm is needed to solve the now defined problems.

TOTAL VARIATION REGULARIZATION

An optimization algorithm for solving the TV regularization problem is implemented. This algorithm is presented, and details of the implementation is described along with algorithmic choices and the motivation for these. The application of the algorithm to the AC problem, which motivated this implementation, is discussed. The implementation of the algorithm is tested on a standard CT problem. Finally the application of this algorithm to PCT and the implementation of the TSD and ACD methods are tested to verify that these methods are also implemented correctly, and that optimization algorithm works as expected on the PCT problems.

An optimization algorithm has been implemented such that TV regularization problems can be solved for both the ABT and the PCT methods presented in [chapter 5](#). The optimization algorithm has been implemented in MATLAB, as well as all other code that has been implemented as part of this project. The motivation for choosing MATLAB as the programming language is that it handles matrices efficiently enough for prototyping purposes and the necessary packages and functions already exists. Besides that, it is easy to set up simple examples to demonstrate the effects of a set up and the code is easy to interpret when comparing to pseudo code or the mathematical equations it is based on. For use on data from real life experiments, all of the methods should be extended to 3D and implemented in a more efficient programming language.

6.1 Implementation of Chambolle Pock algorithm

For both the ABT method and the PCT methods an optimization algorithm is the main ingredient in solving the reconstruction problem. A reconstruction

problem usually becomes a large linear system even for small $N \times N$ pixel separated domains. However, since the system matrix A from (2.7) is sparse, the memory needed to store this is reduced dramatically by only storing non-zero elements and their indexes. This method is also applicable for the TS methods, since the system matrix and the entire reconstruction stage is similar to ABT reconstructions.

For the AC methods the system matrix becomes dense since it includes a Fourier transform, so storing this matrix will demand a lot of memory. In order to avoid this, a so called matrix-free system can be set up, where system matrix can be applied to the variables without setting up and storing the entire system matrix. This matrix free formulation gives rise to another problem, which is the choice of optimization algorithm. As mentioned previously TV regularization is the reconstruction method which will be used for all the methods when comparing them, though when introducing the matrix free formulation the optimization algorithm should be able to handle this. In order to have that, an optimization algorithm, which can be used to solve TV regularization problems, has been implemented.

Based on an algorithm presented by Chambolle and Pock [20] and the adaptation to the TV-regularization problems presented in [21], an optimization algorithm for solving the matrix free TV regularization problem has been implemented. This optimization algorithm is referred to as the CP algorithm. In the following, a general formulation of a linear problem that is referred to is $\mathcal{A}v = y$, where \mathcal{A} is the system matrix, v the variables and y the data. The gradient ∇ is should be regarded as the 2D finite difference derivative approximation in directions x_1 and x_2 separately. As proposed in [21] the operator for the TV regularization problem becomes the combination $K = \begin{pmatrix} \mathcal{A} \\ \nabla \end{pmatrix}$. The specific version of the CP algorithm, adjusted to the TV problem, is the ℓ_2^2 -TV CP algorithm, with the pseudo code presented in Algorithm 4 in [21]. Since this algorithm is implemented to handle a matrix free set up, the application of the system matrix \mathcal{A} or it's transpose \mathcal{A}^T to a vector, should be function calls, rather than matrix multiplications, other than that the algorithm is implemented according to the pseudo-code.

To compute the norm of K the power method presented in algorithm 8 in [21] is used. The loop of the power method runs for 30 iterations, which should be enough to for it to have converged. In the simulated experiments for this project, the objects considered are relatively small (in the range of μm) which can make the system matrix applied to a vector, $\mathcal{A}v$, result in very small values. Since storing numbers on a computer has a finite numerical precision, these very small values could affect the result when running the algorithm. To avoid this,

a scalar factor s has been introduced as a parameter of the method, where the linear problem is scaled as such $s\mathcal{A}v = sy$. This lead in a new linear problem $\mathcal{A}^*v = y^*$, with $\mathcal{A}^* = s\mathcal{A}$ and $y^* = sy$, where the solution v is the same as before and therefore this scaling is only a computational need.

In order to stop the iterative algorithm, in an other way than just by running some fixed number number of iterations, a stopping criterion has been added. This stopping criterion uses the relative change of the solution in each step to determine when to stop. For the solution u in step $k + 1$ the relative solution change is measured in the 2-norm as

$$\tilde{u}_{k+1} = \frac{\|u_{k+1} - u_k\|_2}{\|u_k\|_2},$$

and saved for each iteration. For some tolerance, which is a user specified parameter, the algorithm will stop when \tilde{u} becomes smaller than this tolerance.

To verify this implementation it is compared to the MATLAB package TVreg [7]. For this test problem the materials of the grain phantom is set to some fictive values taken from [3]. The background is set to 0, so non-absorbing, and all other material is set to $\beta = 5 \cdot 10^{-11}$, which resembles a weak absorbing material [3]. The ABT method is chosen for this test, since this is the standard CT method. The other physical details of this test are:

- Source:** Energy of the source $E = 40\text{keV}$ or wavelength $\lambda = 0.31\text{\AA}$,
- Detector:** Pixelsize of $1\mu\text{m}$ and 200×200 pixels in total,
- Projections:** 359 evenly distributed angles between 0° and 179° degrees and 572 evenly distributed beams for each angle.
- Photons:** 10^7 detected photons per pixel.

For different choices of the regularization parameter α the problem is solved with the implemented CP algorithm. The algorithm is run for 2000 iterations in this example or until the stopping criterion was met with the tolerance 10^{-6} . The results are shown in Figure 6.1. To evaluate the convergence of the algorithm, the relative change of the solution \tilde{u} , is shown in Figure 6.2. When the relative change of the solution reduces, it is a sign that the algorithm approaches some specific solution, which a necessary, but not sufficient condition for convergence. Solutions of this problem solved with the TVreg package is presented in Figure 6.3, to see if the results from this well established algorithm are similar to the results from the implemented CP algorithm.

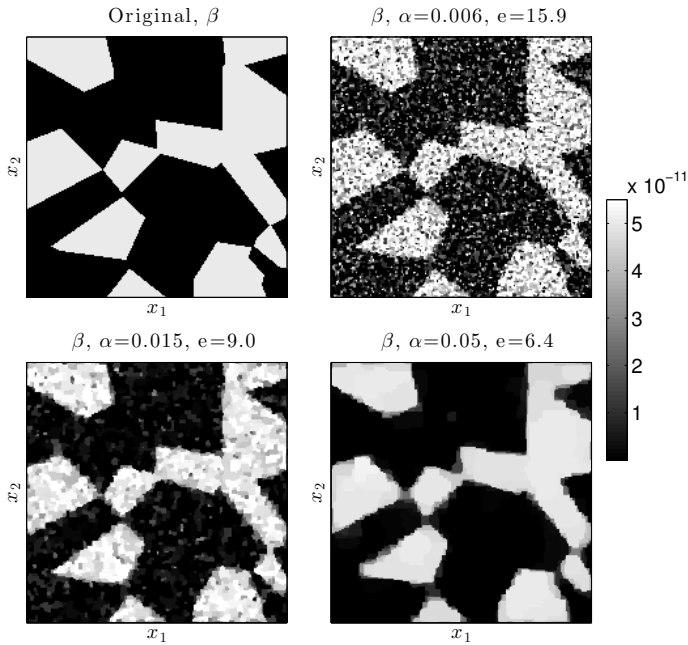


Figure 6.1: Solutions of the ABT problem with a fictive material on a non-absorbing background. The solution algorithm is the implemented CP algorithm where a scaling of $s = 10^4$ has been used. Different choices of the regularization parameter α shown.

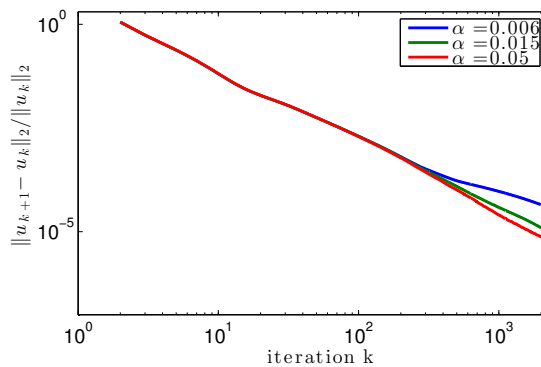


Figure 6.2: Relative solution change for each step of the CP algorithm, as the 2-norm of the solution difference between iterative steps. Illustrated for different choices of the regularization parameter α .

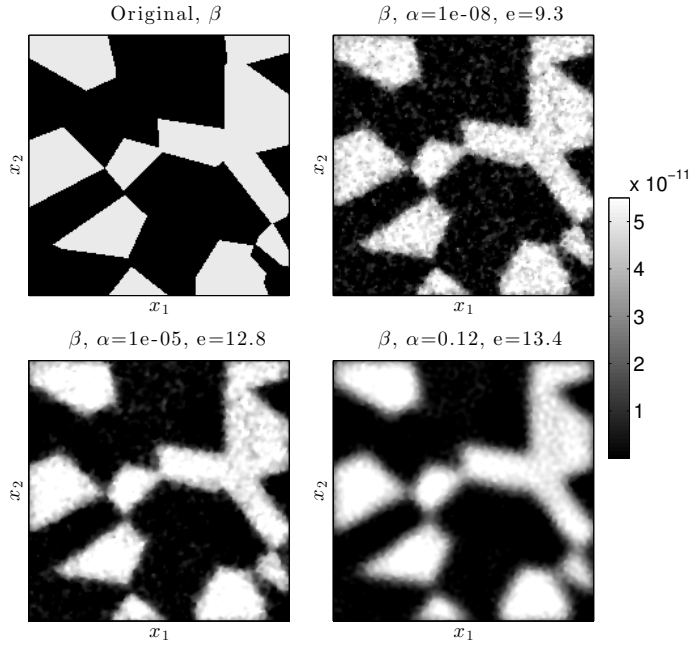


Figure 6.3: Solutions of the ABT problem with a fictive material on a non-absorbing background. The TVreg solution method has been used to solve the problem for different choices of the regularization parameter α .

These tests shows that the implemented CP algorithm can be used to solve TV regularization problems, especially the CT problem. The implemented CP algorithm is seen to give results comparable to the results produced by a well established TV regularization solver, and therefore the implementation of this solver is expected to be correct. The tests also shows the effect of the regularization parameter which smooths the solution in some sense. In [chapter 7](#) several simulations are shown where a regularization parameter has to be chosen. These simulations has been carried out for several choices of the regularization parameter, and solutions presented here is chosen as a "best" solution. The best solution is chosen based on the error measure $e(u)$ (2.5) combined with visual inspection of results, where distinction between materials and reduction of noise and artifacts are considered.

6.2 TV for Phase contrast data

The implemented CP algorithm is tested for the two phase contrast methods TSD and ACD, in order to verify the implementation of these method. In order to have a reference for the results the material set to the same fictive material as in [section 6.1](#), that is $\beta = 5 \cdot 10^{-11}$. This number is taken from Kostenko [3] where it together with $\delta = 5 \cdot 10^{-9}$ is referred to as a weak phase problem. These fictive parameters has been used to produce some good results for the ACD method, therefore this also tested here to check if the implemented ACD method works as expected. At the same time the same problem is solved using the TSD method and ABT method in order to see the differences of between the solutions for this fictive problem. The details of the experiment is the same as in [section 6.1](#) and the PCT data is acquired from a distance of $R = 1\text{m}$. The methods are run for 400 iterations or until the relative solution change becomes lower than the tolerance of 10^{-5} . The results from using these three methods are visualized in [Figure 6.5](#). The relative change of each of the solutions is visualized in [Figure 6.4](#).

The tests of PCT methods on this fictive material test problem shows that ACD and TSD method can be used to solve this problem. In the results from chapter 5 in Kostenko [3] an other phantom is used, but with respect to all other aspects the experiment is the same as the one presented above. Comparing the solutions it seem that, for this experiment, the combined method can give good results and as seen in [Figure 6.5](#), the TSD and ACD methods gives similar results.

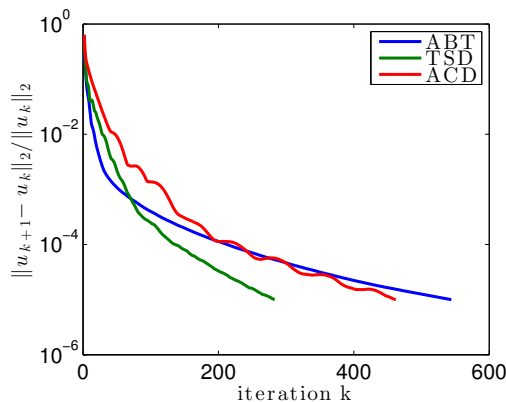


Figure 6.4: Relative change of the solution when solving the fictive problem with the three methods shown in [Figure 6.5](#). The problem is solved using the implemented CP algorithm.

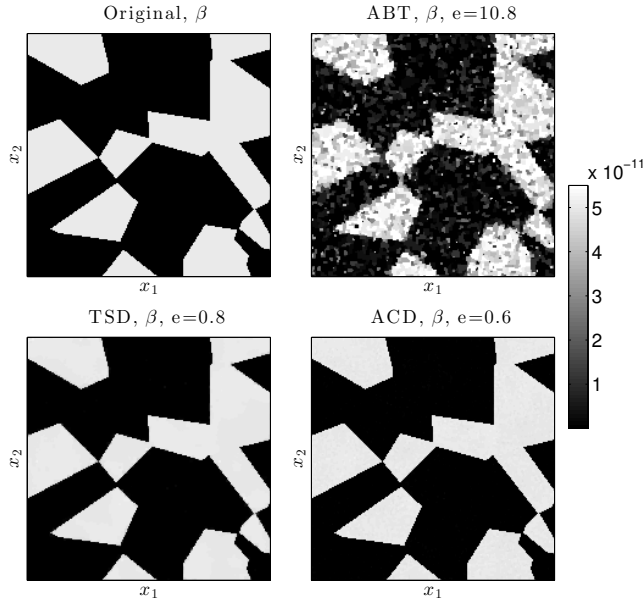


Figure 6.5: Test of the ACD method on a problem with the grain phantom and the fictive material parameters, $\beta = 5 \cdot 10^{-11}$ and $\beta = 5 \cdot 10^{-11}$, taken from Kostenko [3]. The problem is also solved using the ABT method and TSD method in order to see if they solve the problem as expected and to compare the different methods. Regularization parameters for the three solutions were set to: $\alpha_{\text{ABT}} = 0.3$, $\alpha_{\text{TSD}} = 0.3$ and $\alpha_{\text{ACD}} = 1.0$. The implemented CP algorithm has been used to solve the problem for each method.

6.3 Summary

An optimization algorithm for Total Variation regularization has been implemented. The algorithm, first presented by Chambolle and Pock [20], has been adjusted for the TV problem as in [21], and finally implemented such that it can handle problems defined in a matrix-free sense. The choice of implementing a matrix version was motivated by the ACD problem, where the large system matrix becomes dense. The implementation has been tested and compared to a well established TV regularization solver to verify the results. Finally the implemented TSD and ACD methods are tested with the newly implemented algorithm, to validate the implementation of these.

Several things could be done to optimize this TV algorithm implementation, including the suggested preconditioning [20], calculation of the duality gap as a

stopping criterion and a possibility of adding constraints to the problem, such as for example non-negativity constraints.

SIMULATIONS

Simulations of physical experiments which demonstrates different aspects of the PCT methods in relation to the experimental settings. The four PCT methods are tested and compared with each other and with the classical ABT method. First the ABT method is compared to the TS method, to show the strength of PCT in some specific experiments. Next the two PCT methods, TS and AC, are compared for different materials to test if the material properties of the object determines which method is most advantageous. Finally the TS and AC method is compared for different noise levels, that is simulations with few versus many detected photons per pixel to see if one method handles noise better than the other.

The four implemented PCT method is now ready to be used to simulate physical experiments in order to test their forces and limits. All the experiments are 2D examples, but the results can be generalized to real life 3D experiments. The idea behind these experiments is to test for which problems the phase contrast tomographic (PCT) methods can give better results than with the standard absorption based tomographic (ABT) methods. The four different PCT methods are also compared to each other for different problems, to test if there is some experiments where one method would be favourable to the others. Based on the results of such simulated experiments one would be able make suggestions on how to handle real life experiments regarding both data acquisition and data processing.

Since the simulated experiments in this project are modelled to fit with real physical experiments in several aspects, there are a number of parameters for the experiments. Most of these parameters are kept constant for all of the following simulations, since the combinatorial possibilities of changing each one of these would grow rapidly. Some parameters are set to values which would be realistic to achieve on a lab scale X-ray set up, these are the energy, the pixel size, the

number of photons on the detector and the length between the object and the detector. Other parameters, such as the number of pixels and the projection dimensions, are chosen such that the computational effort is not too massive, since the efficiency of the implementations has not been the main focus. The parameters shared by the simulations are listed below:

- Source:** Energy of the source $E = 40\text{keV}$ or wavelength $\lambda = 0.31\text{\AA}$,
- Photons:** 10^5 detected photons per pixel.
- Distances:** For the ABT method the distance from object to detector R is assumed to be negligible, so $R \sim 0\text{m}$, for the single distance methods, TSD and ACD, the distance set to $R = 0.5\text{m}$ and for the two distance methods, TS2R and AC2R, the two distances are set to $R_1 = 1\text{mm}$ and $R_2 = 0.5\text{m}$.
- Detector:** Pixelsize of $1\mu\text{m}$ and 200×200 pixels in total,
- Projections:** 359 evenly distributed angles between 0° and 179° degrees and 572 evenly distributed beams for each angle.

The distances R_1 and R_2 are chosen such that one distance is relatively far away from the object, where both the refractive and absorbing effects are detectable and one close to object where the absorbing effects are mainly visible.

The phantom used for the simulations is the grain phantom described in [subsection 3.3.1](#), where the background is a polycarbonate background, unless otherwise mentioned, and the grains consists of two other materials. The refractive index decrement and absorption index for the different materials can be found in [Table 3.1](#). For the duality methods, TSD and ACD, the proportionality constant σ is a parameter of the methods. For experiment where specific materials is expected in the object this value could be set exactly. By testing for different choices of this parameter, it is seen that it is not so important if σ is chosen to be the exact value, but within $\pm 50\%$ it gives similar results. In these simulations this constant is set to the exact value of the grain material where σ is lowest. The width of the detector is the length of the diagonal of the object, though still some effect could affect the results near the boundary, so in order to avoid these effects a frame of zeros has been added to the object, which is then removed again when a solution is found.

In all of these tests the implemented CP algorithm has been used for the solving the TV regularization problems. It has been set to run for 2000 iterations or until the stopping criterion, with tolerance 10^{-5} , was met.

The different reconstructions are compared visually, and in order to also quantify the correctness of the reconstructions numerically, a relative error measure e (as the one from [subsection 2.1.1](#) equation (2.5)) is used to compare the results to the ground truths. The results are visualized as images next to images of the ground truths, and to make the results comparable to the ground truths, the color intensity range on these images has been set to $\pm 10\%$ of the ground truth. Intensities on any of the solutions above or below these values are truncated to the nearest value with the intensity range. When visualizing both the β and δ values, an intensity range

7.1 Classical CT vs phase contrast tomography

Classical computed tomography, here called absorption based tomography (ABT) is compared to the two stage (TS) phase contrast tomographic method, where the two stages are a phase retrieval stage and a reconstruction stage. The two implemented TS methods, TSD and TS2R, are tested for two different problems. For the first problem the material in the grains consists of silicon and magnesium, which have similar refraction and absorption properties (see [Table 3.1](#)). For the second problem the grains consists two materials which are even more similar, in the sense of β and δ , namely silicon and aluminium. Because silicon and aluminium are more identical than silicon and magnesium, this second problem is considered as a harder problem since distinction between the different materials is desired. The TSD method for the two problems is shown in [Figure 7.1](#) and [7.2](#) and the TS2R method for the same two problem is shown in [Figure 7.3](#) and [7.4](#).

These simulated experiments has shown that for materials like these, the TS methods can give better results than the classical ABT method. The ABT method gave better results for the harder problem and this makes sense since aluminium is more absorbing than magnesium which makes it easier to distinguish from the noise and the background. For the easier problem with silicon and magnesium, both the TSD method and TS2R method gave good results where the distinction between the two materials where clear, though the TSD method had problems setting the level of the background material. For the harder problem the TSD method gave a result where the distinction between silicon and aluminium was difficult, but the TS2R method gave a result where the refractive index decrement could used to distinguish between the two. It should be noted that the TS2R method uses twice the amount of the data, intensity measurements from two distances, so this could be one reason why it gives better results.

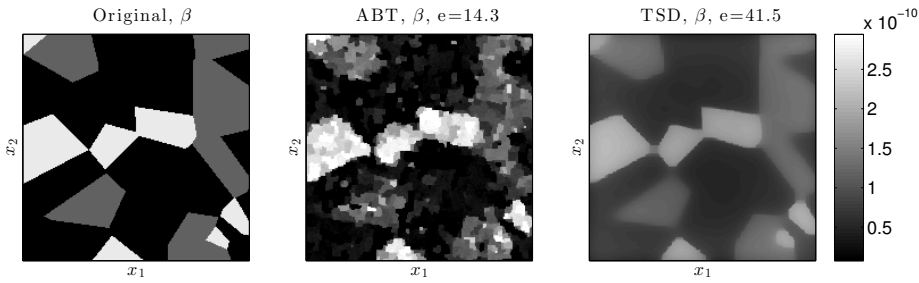


Figure 7.1: Comparison of ABT and TSD. The material in the grains are silicon(highest β) and magnesium. The regularization parameters are set to $\alpha_{\text{ABT}} = 1.4$ and $\alpha_{\text{TSD}} = 0.8$. On the TSD result the distinction between the different materials in the grains is clear, even the small parts, though the background level of background is too high. The ABT result is affected by the noise and it is hard to determine the exact size of the grains and the exact material in each one of them.

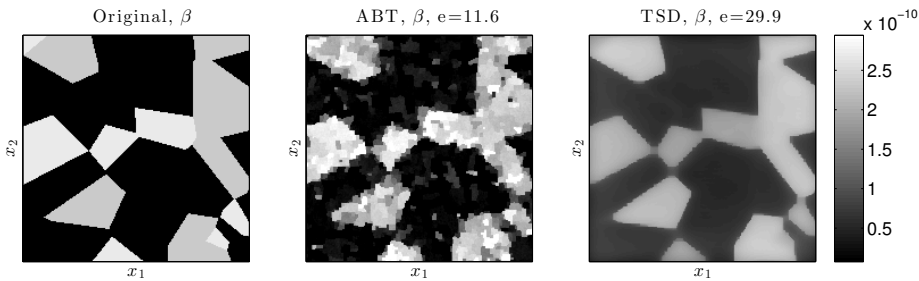


Figure 7.2: Comparison of ABT and TSD. The material in the grains are silicon(highest β) and aluminium. The regularization parameters are set to $\alpha_{\text{ABT}} = 1.4$ and $\alpha_{\text{TSD}} = 0.7$. The ABT result is affected by the noise, but the edges of the grains are somewhat detectable. The TSD result shows a clear edge between background and grains, though the background level is too high and the material distinction between the different grains is not so obvious.

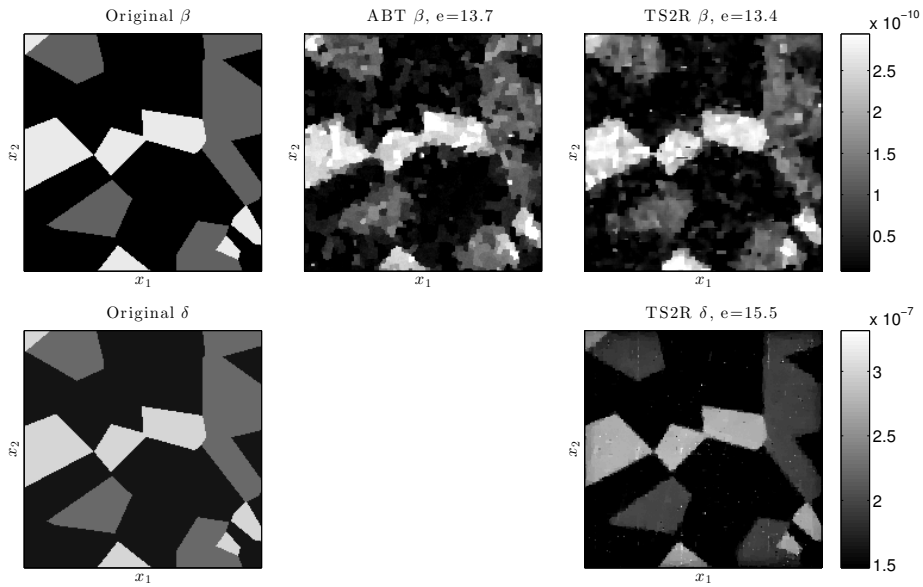


Figure 7.3: Comparison of ABT and TS2R. The material in the grains are silicon(highest β and highest δ) and magnesium. The regularization parameters were set to $\alpha_{\text{ABT}} = 1.4$, $\alpha_{\text{TS2R-}\beta} = 0.5$ and $\alpha_{\text{TS2R-}\delta} = 130$. The ABT solution only has a β as result, since this method does not calculate the refractive index decrement. From the ABT result it is more or less possible to determine what material is located where, but the edges and sizes of the grains are hard to determine. The TS2R result for β is similar to the result from ABT and the δ result shows a clear distinction between the materials of the grains and from the background, though the levels of the silicon and aluminium grains are a bit lower.

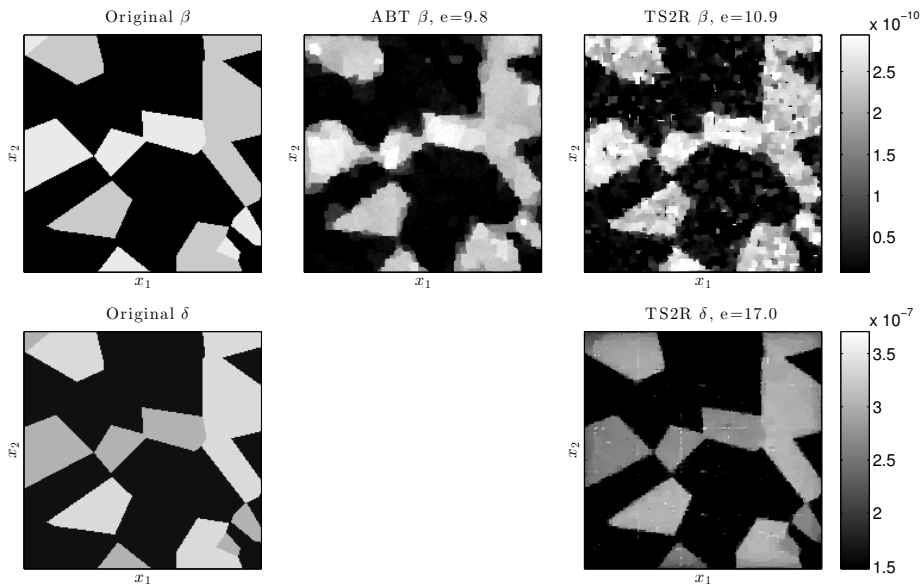


Figure 7.4: Comparison of ABT and TS2R. The material in the grains are silicon (highest β and lowest δ) and aluminium. The regularization parameters were set to $\alpha_{\text{ABT}} = 1.4$, $\alpha_{\text{TS2R-}\beta} = 0.5$ and $\alpha_{\text{TS2R-}\delta} = 130$. The ABT method gives a result where it is possible to distinguish the grains from the background, but still with some problems on the grain edges and clear problems when it comes to distinguishing between the materials of the grains. The TS2R result for β is affected by noise and it is not clear what material the different grains are made of. However the TS2R result for δ gives clear edges for the grains and here it is possible to determine which grains consist of which material.

For materials with higher absorption index, β , the ABT method will give better results. The CTF method is based on that the absorption data is weak ($B_\theta(t) \ll 1$), so for problems with materials where this does not hold, it should be noted that the ABT method would be preferable to the TSD or TS2R method. However for the examples presented in this section the advantage of using PCT is clear.

7.2 PCT methods for different materials

Now that the advantage of using phase contrast tomography has been shown, the different PCT methods are compared for different materials. The four methods TSD, ACD, TS2R and AC2R has been implemented, and these are used to solve different problems to test which method is advantageous for which type of problem.

The methods are tested against each other for different materials to see how they handle different problem types. Three different problems has been defined where each of the different methods are tested to see how they handle the problems compared to each other. The three problem are defined by the size of the absorption index β , such that there is a low level absorption problem, $\beta \sim 10^{-11}$, and medium level absorption problem, $\beta \sim 10^{-10}$, and a high level absorption problem, $\beta \sim 10^{-8}$.

- 1) The first problem has got silicon and aluminium grains, which are both materials of a medium level of absorption. These materials are used to test whether the AC methods can solve this harder problem as good as or better than the TS method did in the previous section.
- 2) The second problem is consists of low level absorbing materials. For this problem the background was changed to a zero absorbing and refracting background, and the grains were set to materials polycarbonate and carbon(in diamond form). This problem was set up to see how these method performs, compared to each other, when the material is very low absorbing. For this very low absorbing problem it would be difficult, to get good results using the absorption based method without having to emit and detect a lot more photons.
- 3) The third problem consists of grains with copper and iron. Both of these materials are high level absorbing materials. This will make it a hard

problem for all of the PCT methods, since they are all build on the CTF method which has an assumption of a weakly absorbing object. Therefore this problem will show which of the methods that handles the difficulties in a problem with high absorbing materials best.

The results from using the CP algorithm on the PCT methods for the different problems are visualized in [Figure 7.5 - 7.8](#).

Carrying out these simulations, it became clear that the AC2R method had some difficulties reconstructing both the absorption index and the refractive index decrement simultaneously. When choosing the regularization parameter α for this method, it could either be chosen relatively low, which is the case for [Figure 7.6](#). This choice makes the values of the δ affected by noise and the result becomes some very small values, without being regularized. The β solution for a relatively low α is similar to the TS2R solution. α can also be chosen as a relatively high value (100), which will make the β solution very blurry, going toward a constant solution. This will affect the δ values for each iteration of the CP algorithm, which then also change to a blurry result, far from the solution we seek. Choosing α in between these two cases resulted in either "over-regulated" β solutions with small δ solutions, or blurry β and δ solutions far from the real solutions. Based on these observations it seem that when solving for the both the δ and β index at the same time, it is not possible to chose a single α which will give good results for both δ and β . So as it is here the AC2R method has some problems and comparisons between this and TS2R are therefore not shown for problems two and three. One approach to handle this, could be to choose individual regularization parameters for each of the two indexes or in some other way handle it by weighting the variables.

The results produced with the ACD method shows some undesired artifacts for the medium and high level absorption problems. These artifacts are line or net structures which are mostly seen in the grains. When solving a problem like this with a regularization method, any undesired artifacts could either dominate the nearby pixels or the artifacts could be dominated by the nearby pixels. The latter is off course desired in order to get rid of the undesired artifacts, but the effect depends on the extend of the artifacts. The grain edges on the ACD results are clear as well as the distinction between grains and the background. The TSD results are blurry and the edges are not completely clear.

Overall the TS2R method seem most advantageous if data is recorded with two detector distances. With one detector distance TSD and ACD both have problems with artifacts and blurry grain edges, for the high level absorption problem, so one is not advantageous to the other. Due to these problems, it is not possible to distinguish

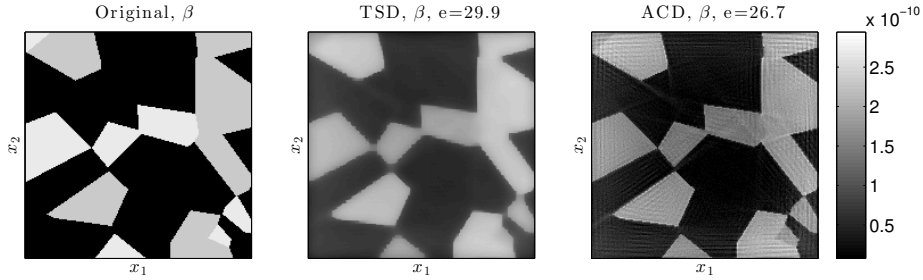


Figure 7.5: Comparison of the TSD and ACD methods. The phantom consists of grains with silicon(highest β) and aluminium. The regularization parameters are set to $\alpha_{\text{TSD}} = 0.7$ and $\alpha_{\text{ACD}} = 3$. On the TSD result it is easy to distinguish between background from the grains, though the level of the background is too high. The grains seem to consist of only one material, so distinction between silicon and aluminium is not possible from this result. The ACD result suffers from artifacts especially closer to the boundary of the object. The edges between the grains and the background are clear, but it is hard to distinguish between the materials of the grains.

the copper grains from the iron grains.

For the medium level absorption problem the TSD result is piecewise constant, but the background level is too high and grain edges are slightly blurry. The ACD method has some undesired artifacts, but besides that the background level and grain edges are more precise. On the ACD result it is, for some grains, possible to distinguish between the different materials, which in total makes ACD slightly advantageous for the medium level problem.

For the low absorption level problem, the grains in the TSD result are blurry as well as their edges, though the overall level of the background and the grains are close to the original β solution. The ACD result has clear grains and edges, but the level of grains, and especially of the background, is further from the original values than the TSD result. Both methods gives solutions with advantages and disadvantages when compared to each other, so the best method for the low level absorption problem depends on whether sharpness or precise intensity levels is of highest priority.

It should also be mentioned that the ACD method had a much slower change rate than the TSD method, that is the change of the solution for the ACD method for each iteration decreased a lot slower than for the TSD method. This can be seen as a disadvantage of the ACD method, since in several practical application a fast convergence rate highly desirable.

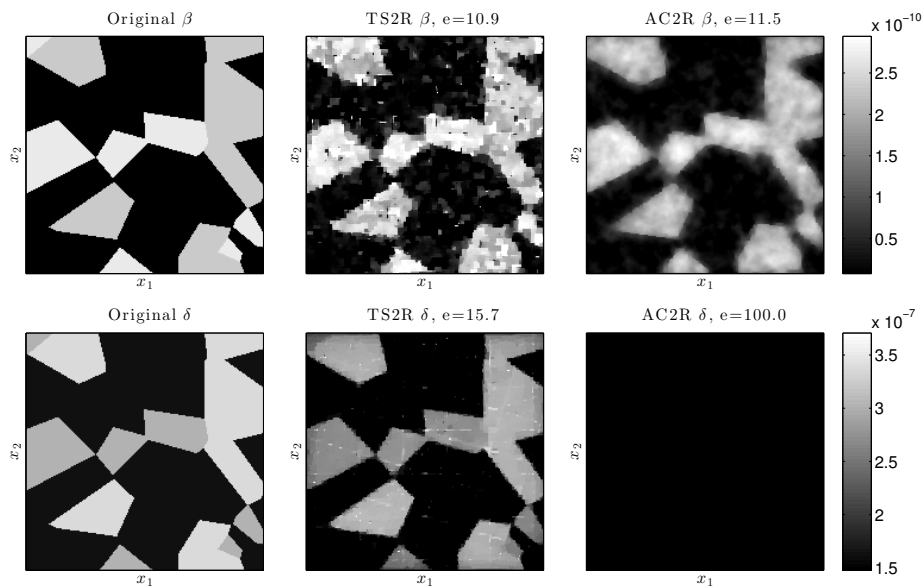


Figure 7.6: Comparison of the TS2R and AC2R methods. The phantom has grains with silicon (highest β and lowest δ) and aluminium. The regularization parameters were set to $\alpha_{\text{TS2R}-\beta} = 0.5$, $\alpha_{\text{TS2R}-\delta} = 130$ and $\alpha_{\text{AC2R}} = 0.1$. The β result from the TS2R method is corrupted by the noise, the grains are detectable, but their edges are blurry and the materials are not distinguishable. However the δ result has a clear edges and from this it is also possible to determine which grains consists of what. The β result from AC2R is also corrupted by noise, but the edges of the grains are clearer than for the TS2R result. The δ result for AC2R method is simply so much smaller than the original values (a factor ~ 30), that the solution cannot be used to tells us anything about the grains.

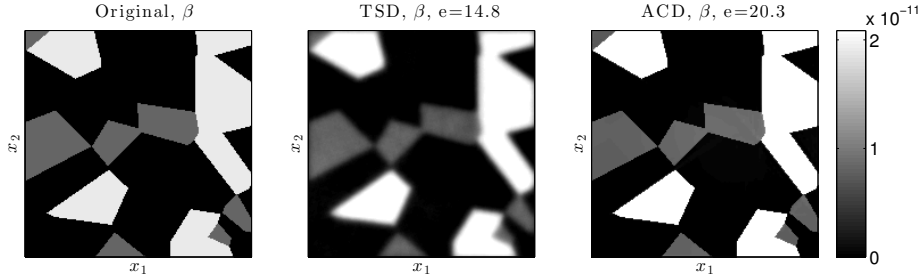


Figure 7.7: Comparison of the TSD and ACD methods. The phantom has grains which consists of polycarbonate and carbon(highest β) in diamond form, and the background is a non-absorbing and non-refracting. The reconstruction parameters was set to $\alpha_{\text{TSD}} = 0.02$ and $\alpha_{\text{ACD}} = 1$. The result from the TSD method is is slightly blurry, but besides this the grain edges are clear and especially the distinction between the two grain materials is very clear. The ACD result is visually very close to the original β image, though the error measure is still around 20, which due to some of the background values being negative instead of 0.

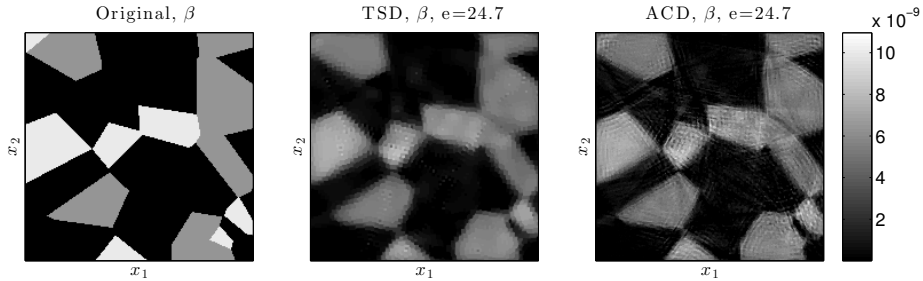


Figure 7.8: Comparison of the TSD and ACD methods. The materials in the grains of the phantom are copper(highest β) and iron. The regularization parameters is set to $\alpha_{\text{TSD}} = 0.5$ and $\alpha_{\text{ACD}} = 12$. The TSD result is affected by small patches/rings which gives a blurring effect. Due to these artifacts the grain edges are blurred and the materials of the grains are indistinguishable. The ACD result also suffers from artifacts which are both small patches and lines through the object. On this solution it not possible distinguish between the material in grains and the grain edges are slightly blurry.

7.3 PCT methods for different noise levels

To test how the TSD and ACD method handles increasing measurement noise best, they are tested for a simulated experiment where the number of detected photons per pixel is reduced. A reduced number of detected photons will make the signal weaker which will make the noise on measurements more dominant. Since the low level absorption problem in the previous section gave the best results for both the TSD and ACD method, this problem is the subject for following noise tests. Here the background is set to a zero absorbing and refracting background, and the grains consists of polycarbonate and carbon in diamond form.

The number photons per pixel is reduced to a significantly lower level of 10^4 detected photons per pixel, as a first problem with increased noise. Such a reduction would mean that the data acquisition time would be reduced significantly.

For the other reduced noise problem, the number of detected photons is once again reduced significantly to 10^3 detected photons per pixel on the detector. This second test will increase the demand for the regularization, since the noise is now increased to a relatively high level.

Together with the results visualized in [Figure 7.7](#), three different noise level experiments has been defined, from relatively low noise (10^5 detected photons per pixel) to relatively high noise (10^3 detected photons per pixel).

The results from the three simulated experiments for with different noise levels can be found in [Figure 7.7](#), [7.9](#) and [7.10](#).

Reducing the detected photons per pixel to a factor 10 smaller, from 10^5 to 10^4 , did not result in solutions which were significantly worse. Since this could speed up the data acquisition, the gain of reducing the photons, for experiments like this, could be very valuable. The further reduction to a relatively low photons count per pixel, 10^3 , has introduced so much noise that both solutions are highly affected by it. A reduction of photons per pixels like this would be most likely not be worth the gain in acquisition time. For the comparison of the TSD and ACD methods, the TSD method handles the noise slightly better, but in general main difference between the two methods is whether the edges of the grains are blurry or the edges are more clear. Based on the fact that the background pixel were better reconstructed by the TSD method, resulting in the lower error measure e , one could argue that the TSD method handles this problem slightly better than the ACD method. However, for increasing noise one method does not seem advantageous to the other.

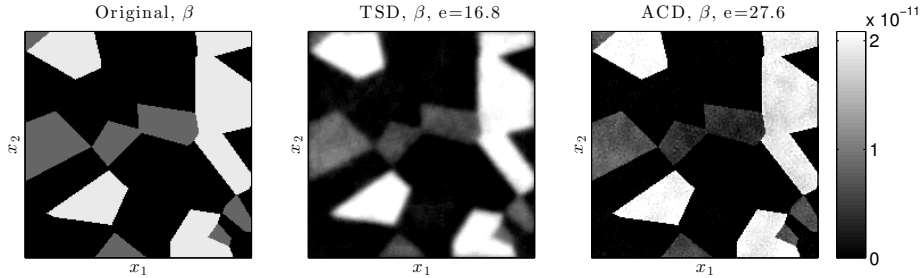


Figure 7.9: Comparison of TSD and ACD. The problem has a zero background, and grains of polycarbonate and carbon in diamond form (highest β). The detected photons per pixel was reduced to 10^4 for this experiment. The regularization parameters were set to $\alpha_{\text{TSD}} = 0.02$ and $\alpha_{\text{ACD}} = 1$. The TSD result is blurry and the edges of grains are not so clear. For the ACD result the grain edges are clear, but some of the background pixels are negative which causes the higher relative error e . For both the TSD and ACD result the polycarbonate grains are mostly affected by noise, especially the grains near the center of the object.

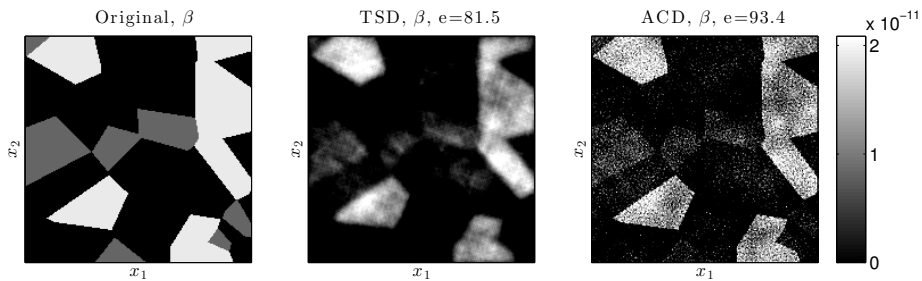


Figure 7.10: Comparison of TSD and ACD. The problem has grains with carbon (highest β) in diamond form and polycarbonate. The background is non-absorbing and non-refracting. The detected photons per pixel is reduced to 10^3 . The regularization parameters were set to $\alpha_{\text{TSD}} = 0.03$ and $\alpha_{\text{ACD}} = 1.1$. Both the TSD and the ACD results are affected by noise and the solutions are relatively far away from the original β , which can also be seen from the high error measures e . The structures of the diamond grains are still reasonably visible, but the polycarbonate grains are barely visible. The TSD result is more blurry than the ACD result which has clearer edges on the diamond grains, though the ACD result has more pixels which are affected by the noise.

7.4 Summary

Simulated experiments are carried out to test PCT against standard ABT and to test and compare the different versions of PCT presented in this project. The TS method have been compared with the ABT method, for two problems, one considered more difficult than the other. The TS methods has produced results which could solve these problems better than the classical ABT method. The more difficult problem needed the TS2R method, which uses data from two detector distances, in order to get results where grains of similar material became distinguishable.

The comparison of the the PCT methods revealed that the AC2R method had some problems when setting it into a TV regularization formulation. The comparison of the TSD and ACD method showed that the results produced by the two methods were similar, but dependant on whether clear grain edges, exact intensity levels in the pixels or the reduction of artifacts are of highest priority, one method could be regarded as slightly more advantageous than the other. The convergence rate of the ACD method was slower than the TSD method, so with efficiency in mind this makes the TSD method preferable. Introduction of more noise to the data did not change this result, but for the problem showed here, a significant reduction of the photons detected, which is a reduction in data acquisition time, could to some extend be done without losing significant detail in the produced results.

7.5 Discussion

The result from using TSD and ACD are similar, though with a few differences which could make one method slightly advantageous to other. In general it seem the gain of going from the TSD method to the regular method TS2R with two detector distances is more valuable. As mentioned, the ACD method converges slower than the TSD method, so by improving the CP implementation such that the duality gap of the method is used as to monitor the convergence and used as a stopping criterion the solutions produced by the ACD method could be improved. Another improvement which could improve all the PCT method is an option to include constraints additional to the TV regularization problem. This could for example be a non-negativity constraint which would reduce the errors introduced by non-realistic negative values.

The TS methods, which has a phase retrieval stage followed by reconstruction stage, can be viewed as an analogue to the FBP method presented in 2.1.1. The phase retrieval stage is essentially a filtering stage, and the TV regularized reconstruction stage is are more advanced back projection. In this view, the AC method filters the solution in each iteration of optimization algorithm instead of just a single filtering of the original intensity signal.

The PCT methods implemented and tested here gives the best results for materials with a relatively low absorption index. These materials are the ones where ABT is mostly affected by noise, so this leaves a room for improvement which can be covered by using the PCT methods.

CONCLUSION AND FUTURE WORK

The aim of this project was to simulate physical phase contrast tomography (PCT) experiments and use these experiments to test and compare different variations of the PCT reconstruction methods. This has been completed, and the results from these comparisons could be the basis for setting up real physical experiments.

The focus for the simulated experiments has been to make simulations where the simulated data resembles real life experiments in different aspects. A forward model for the simulations has been presented and implemented. The model is based on a discrete formulation which can easily be related to real physical units.

Theory behind computed tomography, reconstruction techniques, phase retrieval and phase contrast tomography has been combined to formulate four different PCT reconstruction methods. All of the methods are put into a TV regularization formulation which is chosen as the main reconstruction method for this project. A need for a matrix free optimization algorithm arose since the systems matrices for the AC methods were large and dense. So to handle this, an optimization algorithm for solving matrix free TV regularized problems was implemented and tested.

The simulations showed the advantage of using PCT opposed to using the classical absorption based tomographic (ABT) method. The PCT methods tested produced better results for materials with smaller absorption indexes, which is exactly where ABT method shows weaknesses in terms of measurement noise for example. The AC2R method turned out to have a weakness when using it in a TV regularized setting. The two duality methods TSD and ACD gave result which were similar, but the TSD result had more exact intensity levels in the solutions, where the ACD method had more clear grain edges. For a harder problem, where distinction between similar materials is important,

the TS2R method could be used to give better result, though data from two detector distances is needed for this method. It has also been shown that for some experiments a significant reducing of the number of photons detected per pixel, can be done without losing a significant amount of information in the data.

8.0.1 Future work

The result presented in this project is based on a series of choices regarding the different models and methods. Essentially the discretization of the tomography model, the phase retrieval method and underlying assumptions, the choice of reconstruction method and within this the choice of optimization algorithm, are all aspect where a choice between different options has been made. So all of these choices could be reconsidered and an this could open for an enormous range of possible combinations. Beneath some suggestions to further development and testing of these method, which seem reasonable and useful after having worked with this topic for several months, are listed.

Other phase retrieval techniques, such as the mixed TIE-CTF method [13] can give better results for materials with higher absorption index, so it could be interesting to compare methods based on this to methods based on CTF solely. The linearization when deriving the phase retrieval methods, only includes first order term. Including higher order term could make the model more realistic and hence improve the phase retrieval.

The implemented optimization algorithm could also be improved by including calculation of the duality gap, which would be a more convergence precise stopping criterion. Further options such as a the possibility for including solution constraints, for example a non-negativity constraint, could improve the method and hence the results produced with it.

Finally the tests here are simulations of physical experiments which could be used in laboratory scale experimental set ups. Therefore a more realistic modelling the X-ray sources available in such a setting could be interesting. This could be done by simulating data produced by a source with energy within a narrow energy band rather than just a single energy and wavelength.

Bibliography

- [1] T. M. Buzug. *Computed Tomography: From Photon Statistics to Modern Cone-Beam CT*. Springer, 2008.
- [2] J. Bian, J. H. Siewerdsen, X. Han, E. Y. Sidky, J. L. Prince, C. A. Pelizzari, and X. Pan. Evaluation of sparse-view reconstruction from flat-panel-detector cone-beam ct. *Physics in Medicine and Biology*, 55(22):6575–6599, 2010.
- [3] A. Kostenko. *Phase-contrast x-ray tomography for soft and hard condensed matter*. PhD thesis, Delft University of Technology, September 2013.
- [4] J. Hadamard. Lectures on cauchy’s problem in linear partial differential equations. 1923.
- [5] J. Als-Nielsen and D. McMorrow. *Elements of modern x-ray physics*. Wiley, New York, NY, 2001.
- [6] J. S. Jørgensen. *Sparse Image Reconstruction in Computed Tomography*. PhD thesis, Technical University of Denmark, April 2013.
- [7] P. C. Hansen and M. Saxild-Hansen. Air tools - a matlab package of algebraic iterative reconstruction methods. *J. Comput. Appl. Math.*, 236(8):2167–2178, 2012.
- [8] R. Gordon, R. Bender, and G. T. Herman. Algebraic reconstruction techniques (art) for three-dimensional electron microscopy and x-ray photography. *Journal of Theoretical Biology*, 29(3):471–476+IN1–IN2+477–481, 1970.

- [9] P. C. Hansen. *Discrete Inverse Problems: Insight and Algorithms*. Fundamentals of Algorithms. SIAM, Philadelphia, 2010.
- [10] M. Beister, D. Kolditz, and W. A. Kalender. Iterative reconstruction methods in x-ray ct. *Physica Med.-Eu. J. Medical Physics*, 28(2):94–108, 2012.
- [11] X. Pan, E. Y. Sidky, and M. Vannier. Why do commercial ct scanners still employ traditional, filtered back-projection for image reconstruction? *Inverse Problems*, 25(12):–, 2009.
- [12] P. Cloetens. *Contribution to Phase Contrast Imaging, Reconstruction and Tomography with Hard Synchrotron Radiation*. PhD thesis, Vrije Universiteit Brussel, Faculteit Toegepaste Wetenschappen, March 1999.
- [13] M. Langer, P. Cloetens, J.-P. Guigay, and F. Peyrin. Quantitative comparison of direct phase retrieval algorithms in in-line phase tomography. *Medical Physics*, 35(10):4556–4566, 2008.
- [14] S. Zabler, P. Cloetens, J.-P. Guigay, J. Baruchel, and M. Schlenker. Optimization of phase contrast imaging using hard x rays. *Review of Scientific Instruments*, 76(7):73705–1–7, 2005.
- [15] S. Kuznetsov. X-ray optics calculator, 2014. http://www.ipmt-hpm.ac.ru/xcalc/xcalc/ref_index.php, IMT RAS, Chernogolovka, Russia, [Retrieved May 20 2014].
- [16] J. P. Guigay. Fourier transform analysis of fresnel diffraction patterns and in-line holograms. *Optik*, 49(1):121–125, 1977.
- [17] A. Burvall, U. Lundstrom, P. A. C. Takman, D. H. Larsson, and H. M. Hertz. Phase retrieval in x-ray phase-contrast imaging suitable for tomography. *OPTICS EXPRESS*, 19(11):10359–10376, 2011.
- [18] A. V. Bronnikov. Theory of quantitative phase-contrast computed tomography. *Journal of the optical society of America A-Optics Image Science and Vision*, 19(3):472–480, 2002.
- [19] Amir Beck and Marc Teboulle. A fast iterative shrinkage-thresholding algorithm for linear inverse problems. *SIAM JOURNAL ON IMAGING SCIENCES*, 2(1):183–202, 2009.
- [20] T. Pock and A. Chambolle. Diagonal preconditioning for first order primal-dual algorithms in convex optimization. *Proceedings of the IEEE International Conference on Computer Vision*, pages 1762–1769, 2011.
- [21] Emil Y. Sidky, Jakob Heide Jørgensen, and Xiaochuan Pan. Convex optimization problem prototyping for image reconstruction in computed tomography with the chambolle–pock algorithm. *Physics in Medicine and Biology*, 57(10):3065–3091, 2012.